Electronic Supplementary Material (ESI) for Inorganic Chemistry Frontiers.
This journal is © the Partner Organisations 2022

Electronic Supplementary Information

Synergistic Lewis Acid and Pd Active Sites of Metal-Organic Framework for High Efficient Carbonylation of Methyl Nitrite to Dimethyl Carbonate

Han-Ying Wu,[a,b,c] *Ye-Yan Qin,*[a] *Yi-Hong Xiao,*[b,c] *Jian-Shan Chen,*[a] *Rong Guo,*[a] *Si-Qi Wu,*[a,b,c] *Lei Zhang,*[b,c] *Jian Zhang*[b,c] *and Yuan-Gen Yao*[*,a,b,c]

[a] Key Laboratory of Coal to Ethylene Glycol and Its Related Technology, Fujian Institute of Research on the Structure of Matter, Chinese Academy of Sciences, Fuzhou, 350002, P. R. China

[b] State Key Laboratory of Structural Chemistry, Fujian Institute of Research on the Structure of Matter, Chinese Academy of Sciences, Fuzhou 350002, P. R. China

[c] School of Chemical Sciences, University of Chinese Academy of Sciences, Beijing 100049, P.R. China

[*]Corresponding Author: Y.-G. Yao, E-mail: yyg@fjirsm.ac.cn

Table of Contents

Materials and instrumentation

1,4-benzenedicarboxylic acid (BDC), N, N-Dimethylformamide (DMF), Zirconium (IV) chloride ($ZrCl_4$), Trifluoroacetic acid (TFA) and Palladium acetate ($Pd(OAC)_2$) were purchased from Aladdin Industrial Corporation. Acetone and Methanol were obtained from China National Medicines Corporation Ltd. All chemicals and solvents used in the syntheses were of reagent grade and used without further purification. X-ray diffraction (XRD) analyses were performed with a powder diffractometer (Rigaku) using Cu Kα radiation ($\lambda = 0.154$ nm). Transmission electron microscopy (TEM), high-resolution transmission electron microscope (HRTEM) and high angle annular dark field scanning transmission-electron microscopy (HAADF-STEM) were performed on Field Emission Transmission Electron Microscope (TALOS F200X G2). TEM specimens were prepared by directly drying a drop of the dilute ethanol dispersion solution of the products on the surface of a carbon-coated copper grid. Inductively coupled plasma (ICP) spectroscopy was carried out with an Ultima 2 plasma emission spectrometer from Jobin Yvon. Thermogravimetric analysis (TGA) was performed using a STA449F3 thermogravimetric analyzer with a heating speed of 5 $K \cdot min^{-1}$ from 298 to 1073 K in air. UV–Vis-NIR diffuse reflectance spectra were collected on Lambda 950 spectrophotometer. The reference was $BaSO_4$ and the absorption spectra were obtained using the Kubelka-Munk function. The IR experiments were performed in absorption mode on a FTIR Bruker VERTEX 70. Brunauer-Emmett-Teller (BET) surface areas were calculated from the N_2 adsorption–desorption isotherms obtained using the BET method, which was performed on an Intelligent Gravimetric Sorption Analyzer (IGA100B) at the temperature (77 K) of liquid N_2. X-ray photoelectron spectroscopy (XPS) was performed using an X-ray Photoelectron Spectroscopy (ESCALAB 250Xi) with monochromatic Al Kα X-ray (1486.6 eV) as the excitation source. The binding energies were corrected by C 1s peak at 284.6 eV. Electrochemical Impedance Spectroscopy (EIS) experiments were carried out in a three-electrode system on an electrochemical workstation (Zahner-Zennium IM6). The ^{19}F-NMR spectra were recorded on a Bruker Avance DSX400 spectrometer (9.4 T). NH_3 temperature programmed desorption (NH_3-TPD) were performed in an autochem II

2920. Specifically, 100 mg catalyst was preprocessed under helium at 393 K for 1 h to remover water and other impurities. Subsequently, the sample was exposed to a NH_3-He mixture (10% NH_3) for 1 h after cooling to 323 K under a helium flow, followed by flowing with helium for another 30 min, then the temperature was rise to 673 K by heating rate of 10 $K \cdot min^{-1}$. The signals were recorded by monitoring the desorbed ammonia with a TCD detector. Pyridine infrared (Py-IR) spectrum was carried out in NICOLET iS50 FT-IR. All the samples were activated in the IR cell (1×10^{-3} Pa, 150 °C, 2 h), then cooling to 298 K and the IR spectrum was recorded as a reference. After that, the samples were exposed to pyridine for 20 mins, and switching back into vacuum for 30 mins to remove the physically absorbed pyridine. The FTIR spectrum was recorded using a Bruker Equinox 55 Fourier transform infrared spectrophotometer. And the IR spectra were recorded in the range of 400-4000 cm^{-1}. CO temperature programmed desorption (CO-TPD) were carried out in an autochem II 2920. Typically, 100 mg sample was pretreated under helium at 393 K for 2 h to remover impurities. After cooling to 313 K under a helium flow, the sample was exposed to a CO-He mixture (10% CO) for 1 h. Subsequently, the temperature was rose to 623 K by heating rate of 10 $K \cdot min^{-1}$. The signals were recorded by monitoring the desorbed ammonia with a TCD detector.

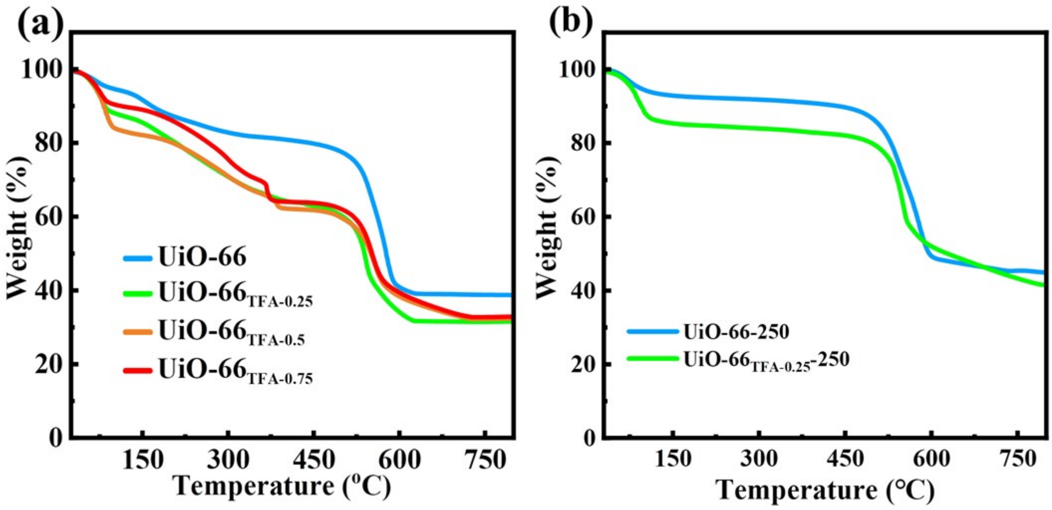

Figure S1. (a) TGA curves of UiO-66$_x$; (b) the TGA curves of UiO-66-250 and UiO-66$_{TFA-0.25}$-250.

In the TGA curves of UiO-66$_x$ (Figure S1(a)), the weight loss before 100°C corresponded with the evaporation of water adsorbed on UiO-66$_x$. The second weight loss in the range of 100-320°C attributed to the removal of DMF from the channel of UiO-66 [1,2], the loss of monocarboxylate ligands, and the dehydroxylation of the Zr_6 cluster [3,4]. As for the activation UiO-66$_x$-250, the first weight loss also was observed before 100°C was attributed to the loss of water adsorbed.

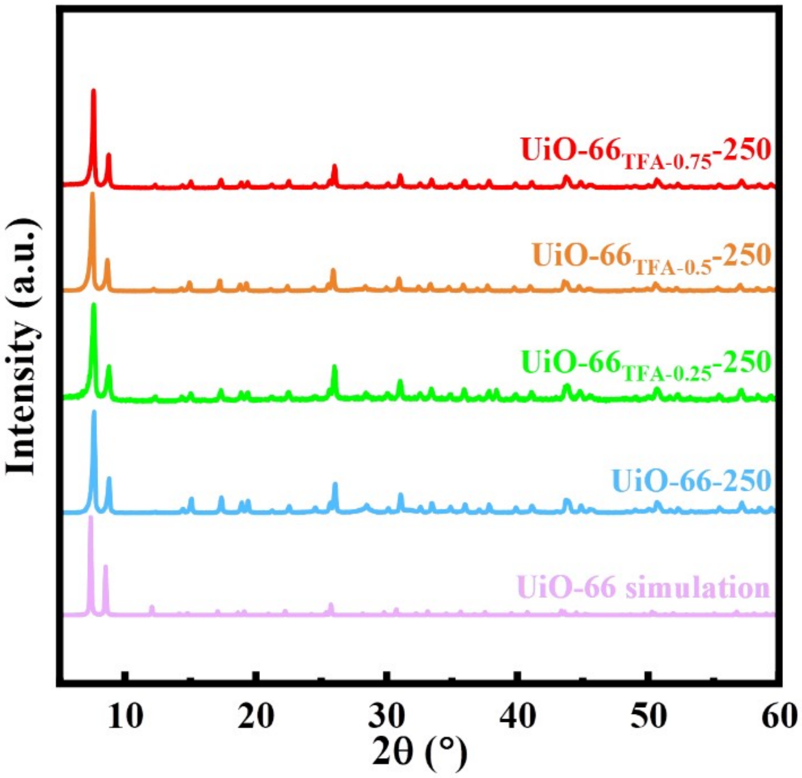

Figure S2. XRD patterns of UiO-66$_x$-250.

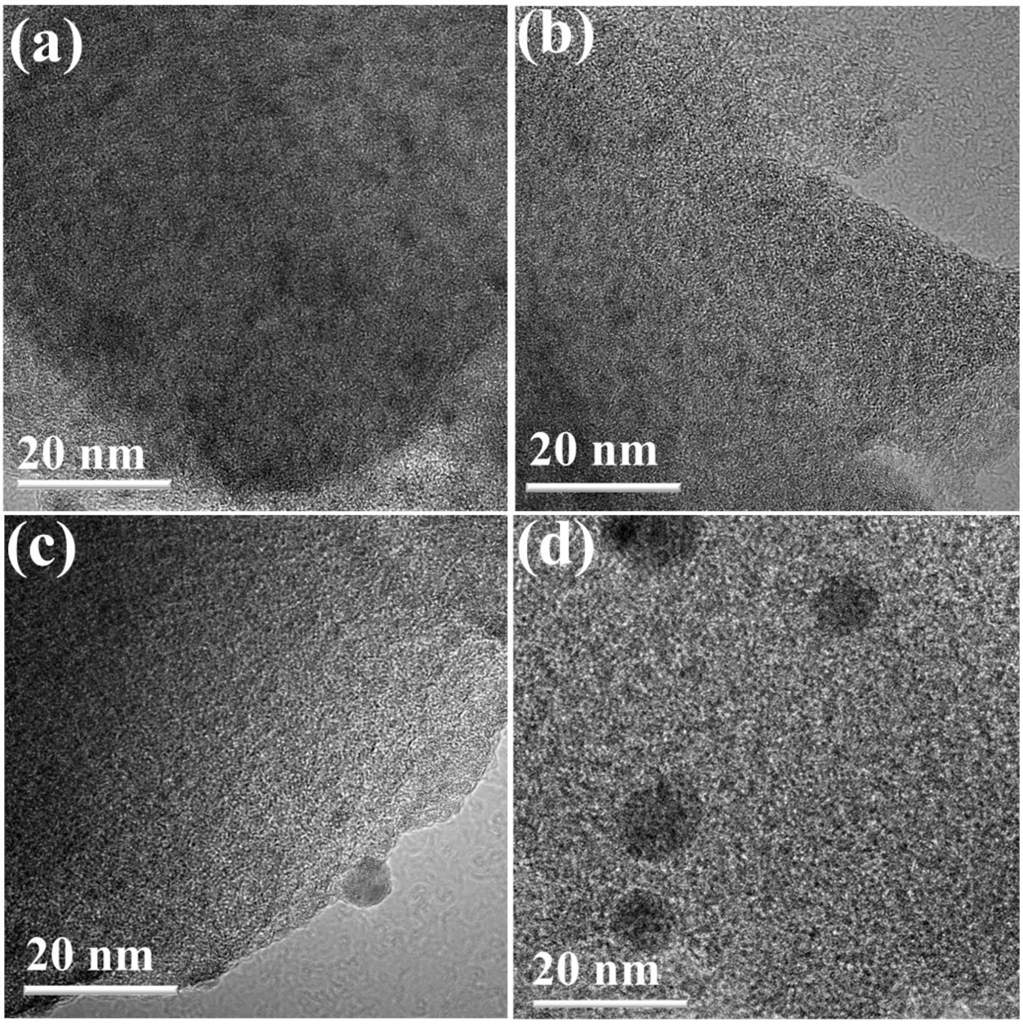

Figure S3. TEM images of (a) Pd-UiO-66-250, (b) Pd-UiO-$66_{TFA-0.25}$-250, (c) Pd-UiO-$66_{TFA-0.5}$-250 and (d) Pd-UiO-$66_{TFA-0.75}$-250.

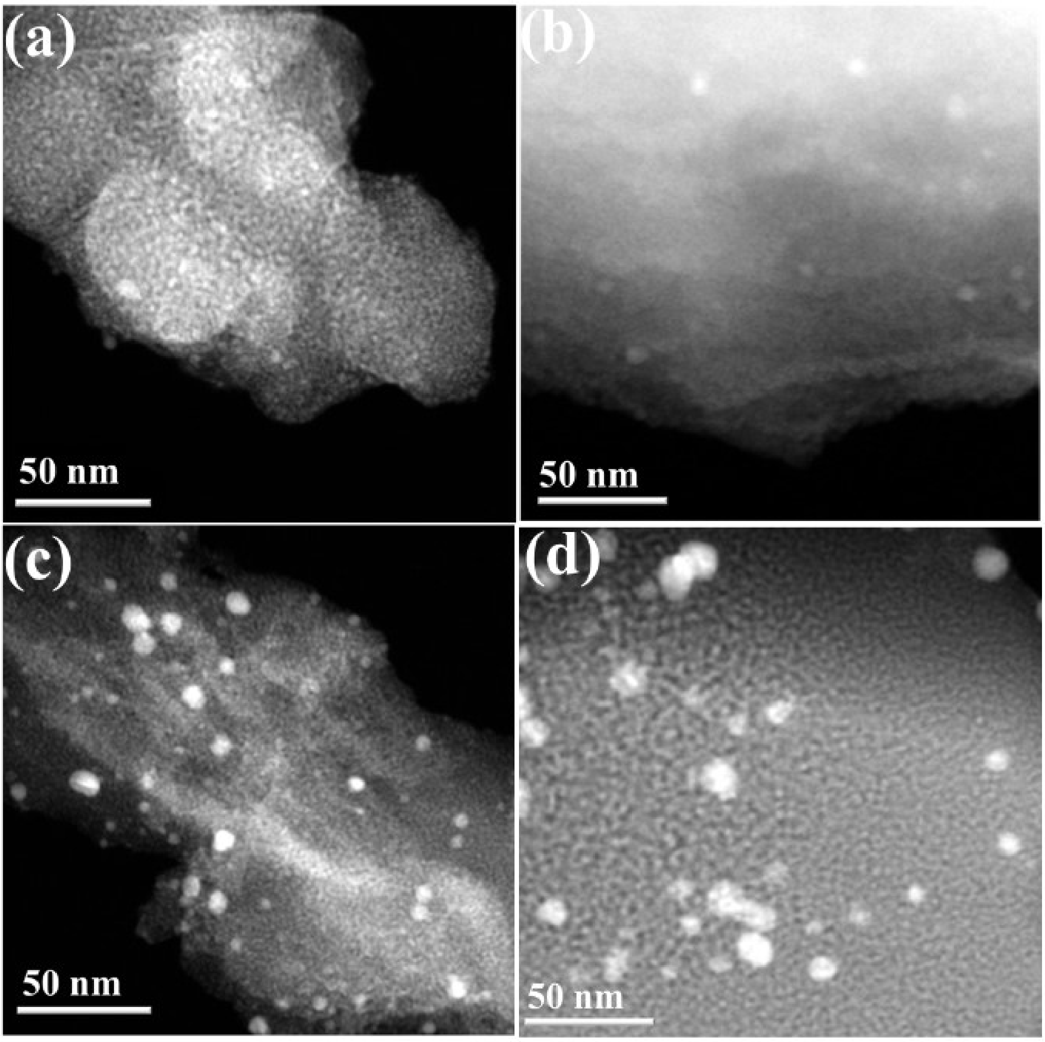

Figure S4. HTEM images of (a) Pd-UiO-66-250, (b) Pd-UiO-66$_{\text{TFA-0.25}}$-250, (c) Pd-UiO-66$_{\text{TFA-0.5}}$-250 and (d) Pd-UiO-66$_{\text{TFA-0.75}}$-250.

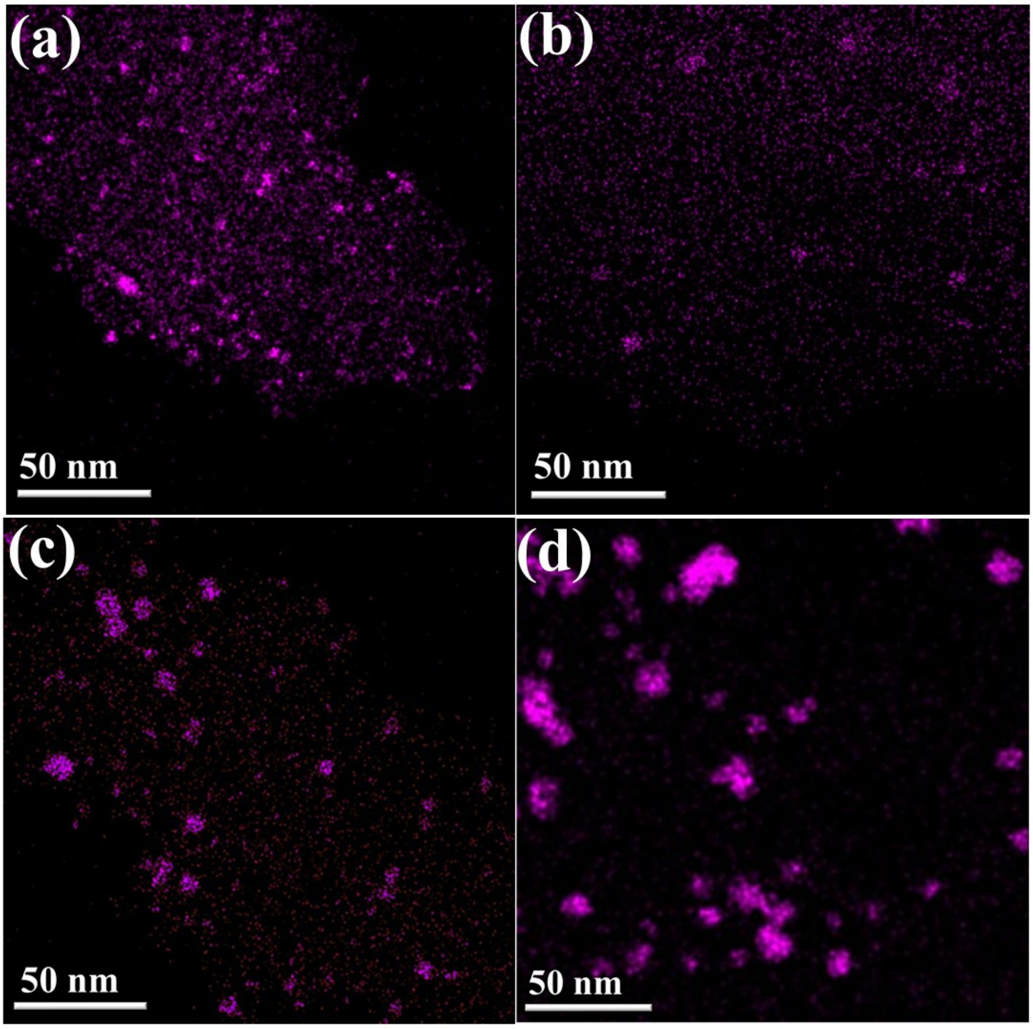

Figure S5. HAADF-STEM images of (a) Pd-UiO-66-250, (b) Pd-UiO-66$_{\text{TFA-0.25}}$-250, (c) Pd-UiO-66$_{\text{TFA-0.5}}$-250 and (d) Pd-UiO-66$_{\text{TFA-0.75}}$-250.

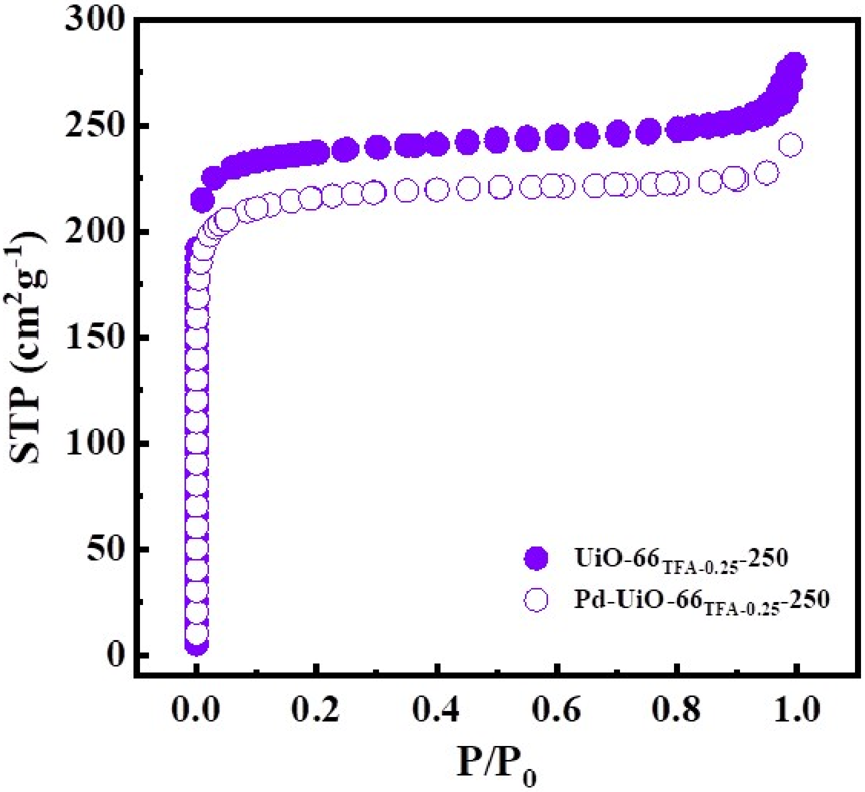

Figure S6. N_2 adsorption isotherms of UiO-66$_{TFA-0.25}$-250 and Pd-UiO-66$_{TFA-0.25}$-250 at 77K.

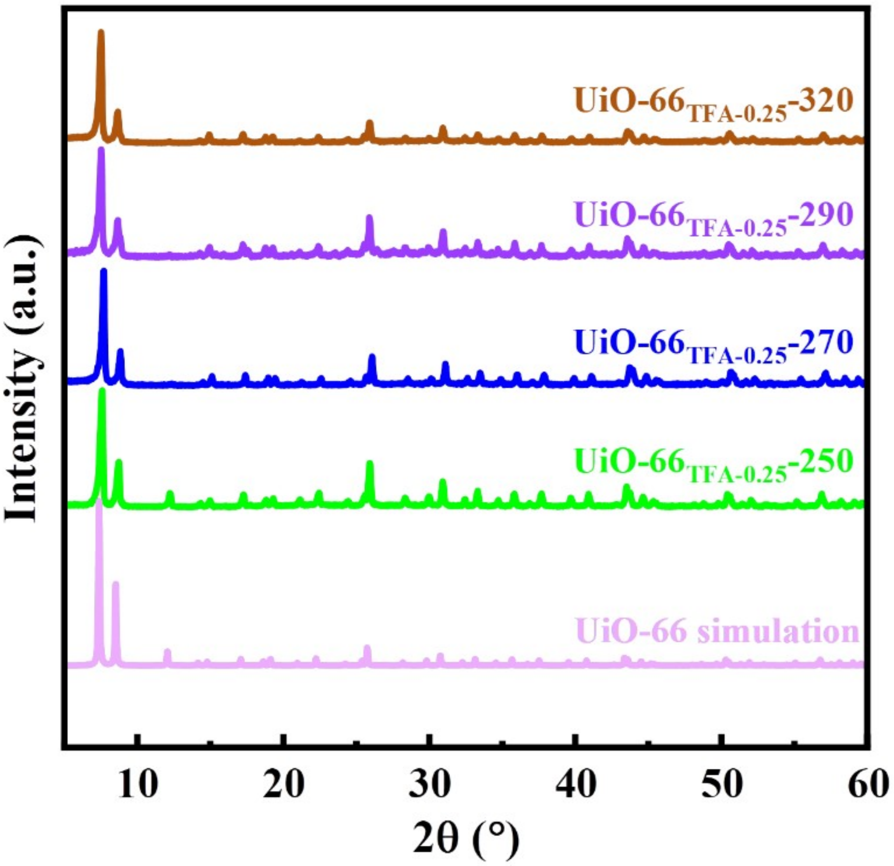

Figure S7. XRD patterns of UiO-66$_{TFA-0.25}$-X.

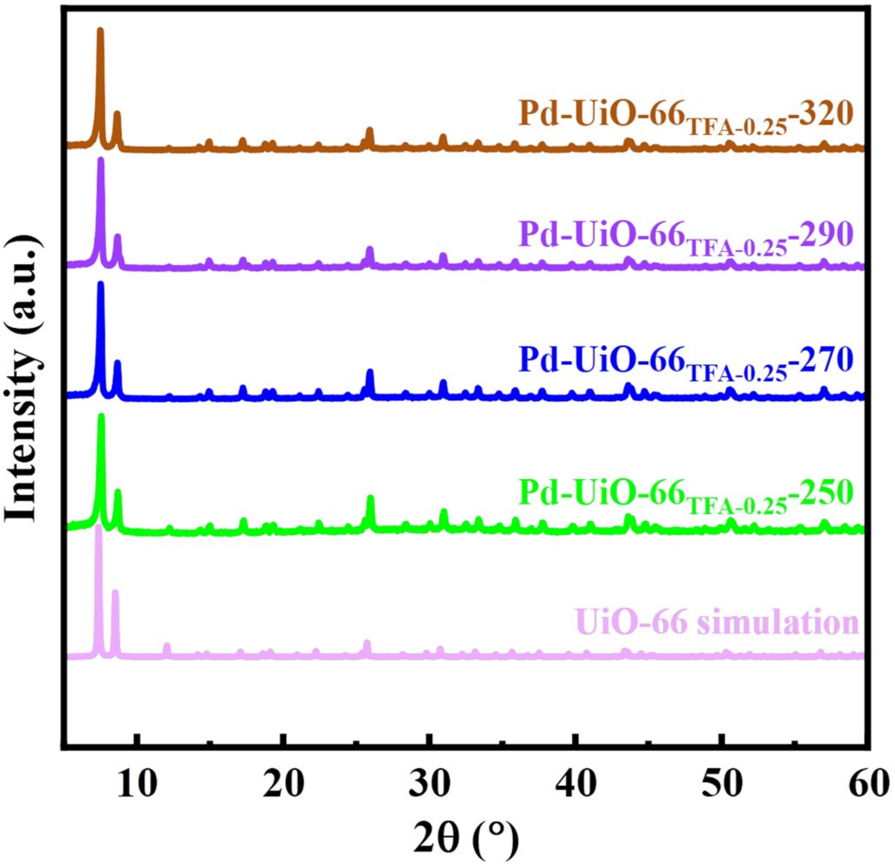

Figure S8. XRD patterns of Pd-UiO-66$_{TFA-0.25}$-X.

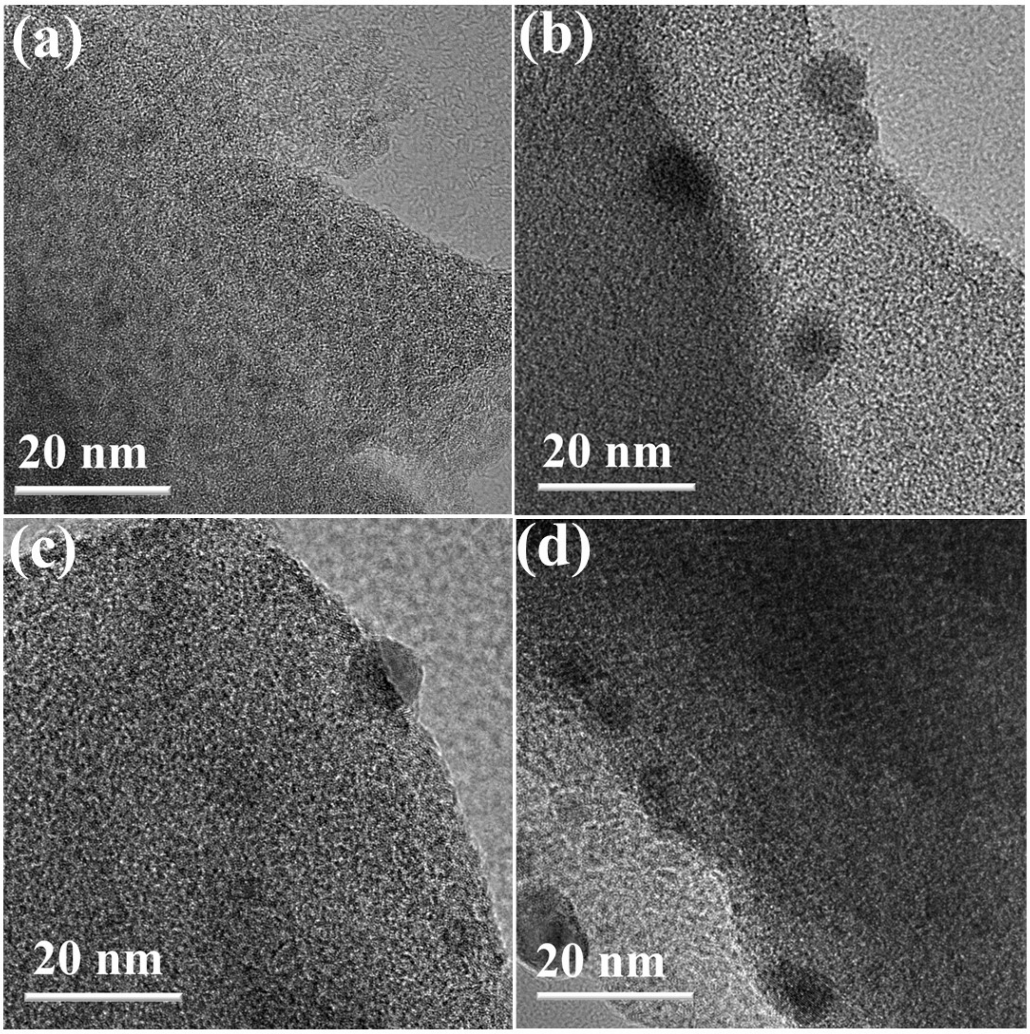

Figure S9. TEM images of (a) Pd-UiO-66$_{TFA-0.25}$-250, (b) Pd-UiO-66$_{TFA-0.25}$-270, (c) Pd-UiO-66$_{TFA-0.25}$-290 and (d) Pd-UiO-66$_{TFA-0.25}$-320.

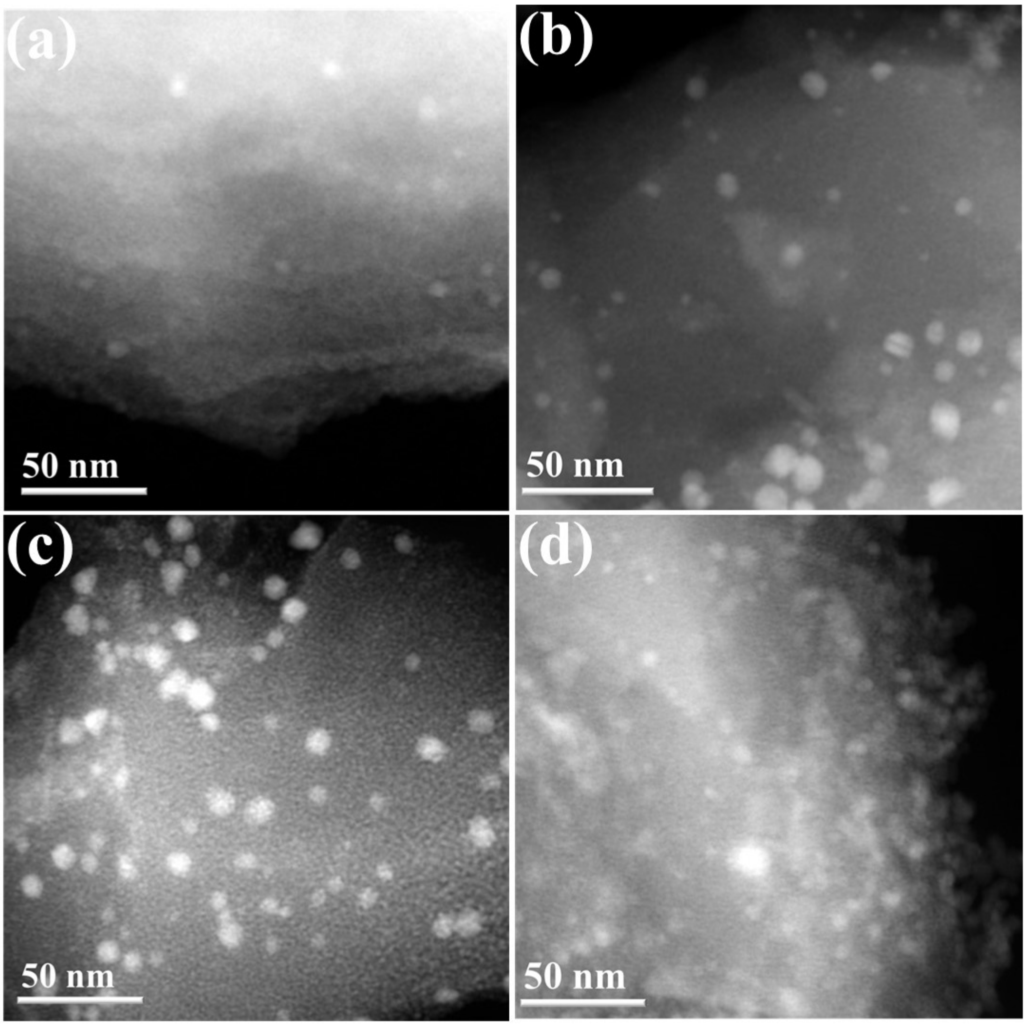

Figure S10. HTEM images of (a) Pd-UiO-66 $_{\text{TFA-0.25}}$-250, (b) Pd-UiO-66$_{\text{TFA-0.25}}$-270, (c) Pd-UiO-66$_{\text{TFA-0.25}}$-290 and (d) Pd-UiO-66$_{\text{TFA-0.25}}$-320.

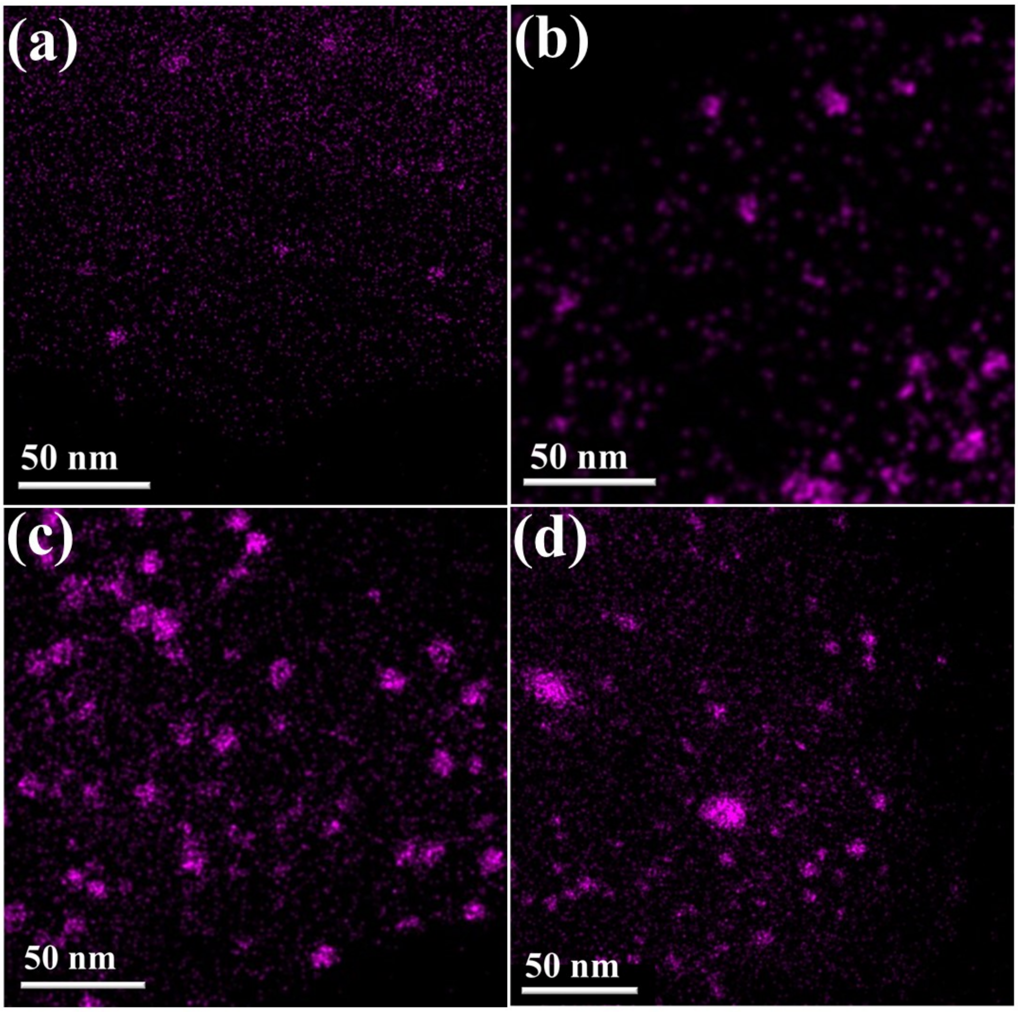

Figure S11. HAADF-STEM images of (a) Pd-UiO-66$_{TFA-0.25}$-250, (b) Pd-UiO-66$_{TFA-0.25}$-270, (c) Pd-UiO-66$_{TFA-0.25}$-290 and (d) Pd-UiO-66$_{TFA-0.25}$-320.

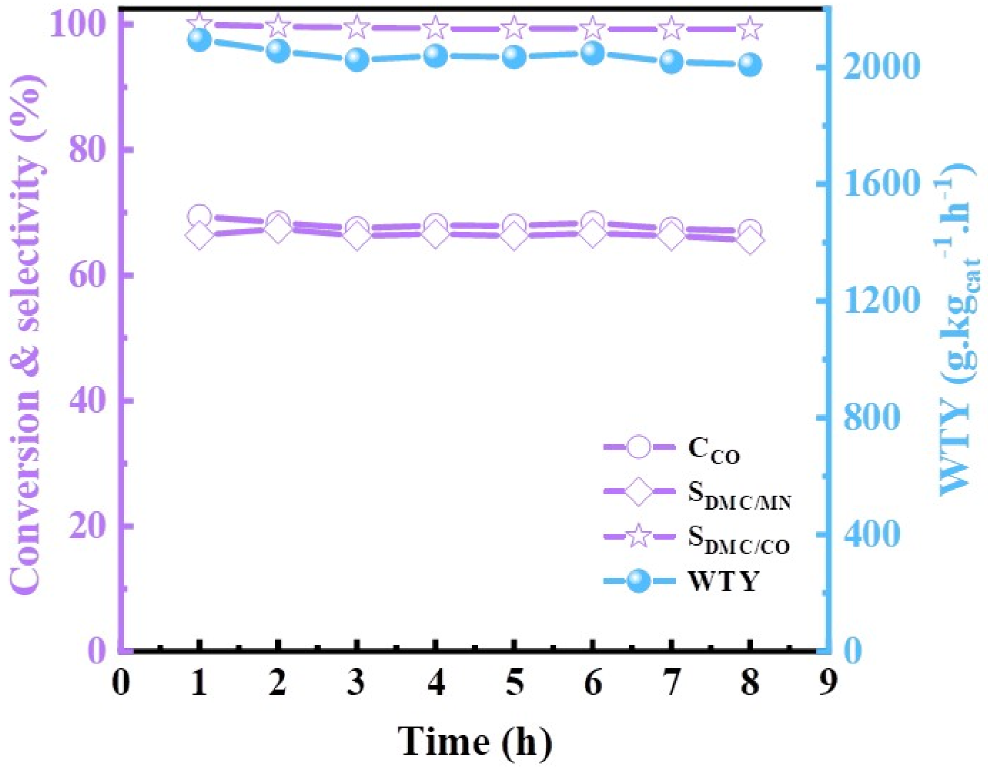

Figure S12. C_{CO}, $S_{DMC/CO}$, $S_{DMC/MN}$ and WTY of DMC in long-term catalytic reaction on Pd-UiO-66$_{TFA\text{-}0.25}$-290 catalyst.

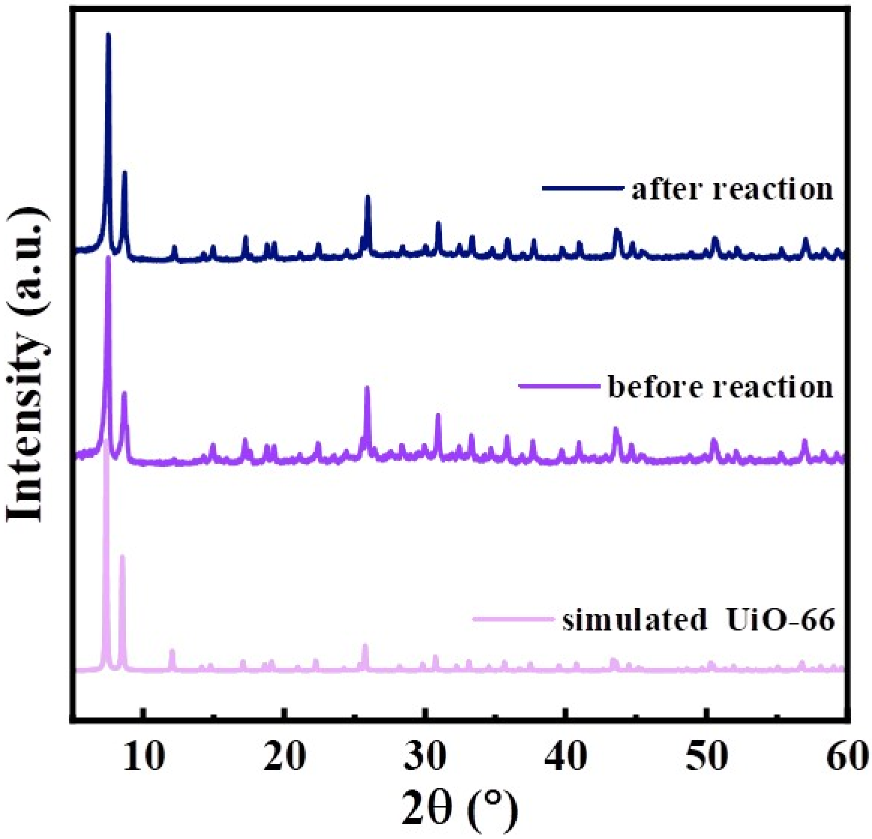

Figure S13. XRD patterns of Pd-UiO-66$_{TFA-0.25}$-290 before and after the reaction.

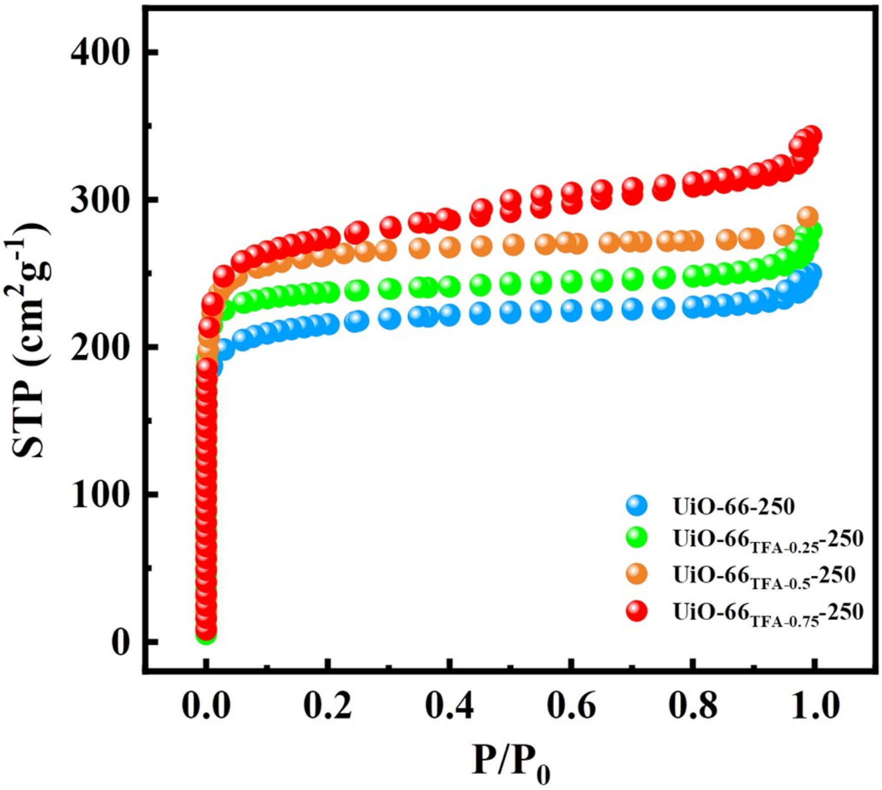

Figure S14. N_2 adsorption isotherms of UiO-66$_x$-250 at 77K.

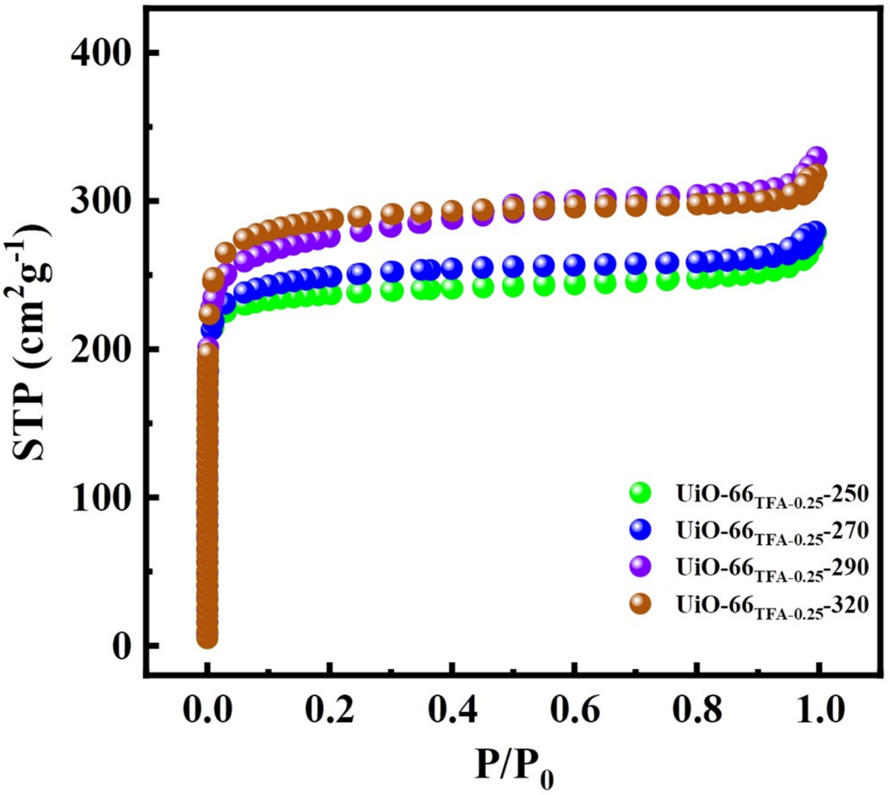

Figure S15. N_2 adsorption isotherms of UiO-66$_{TFA-0.25}$-X at 77K.

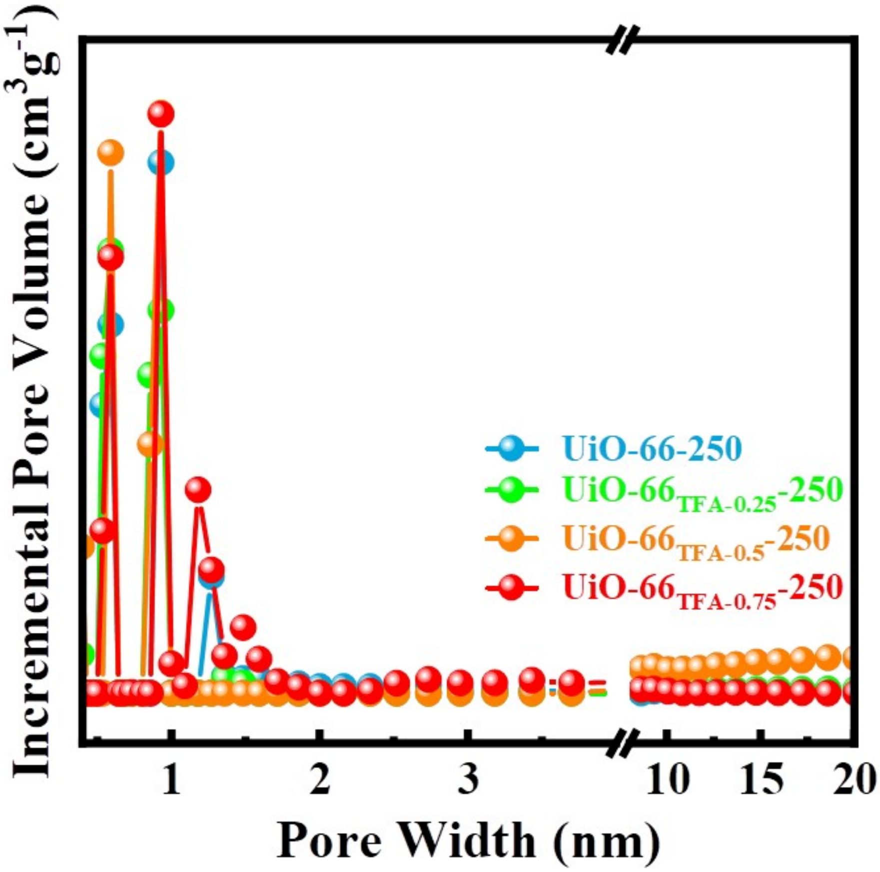

Figure S16. Pores size distribution of UiO-66$_x$-250.

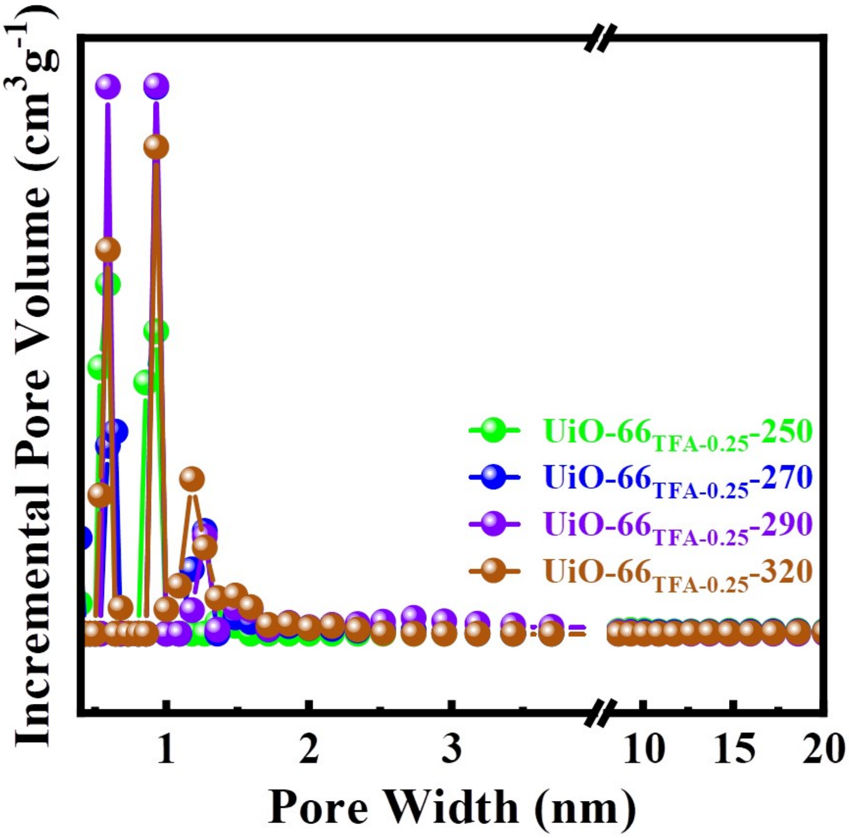

Figure S17. Pores size distribution of UiO-66$_{TFA-0.25}$-X.

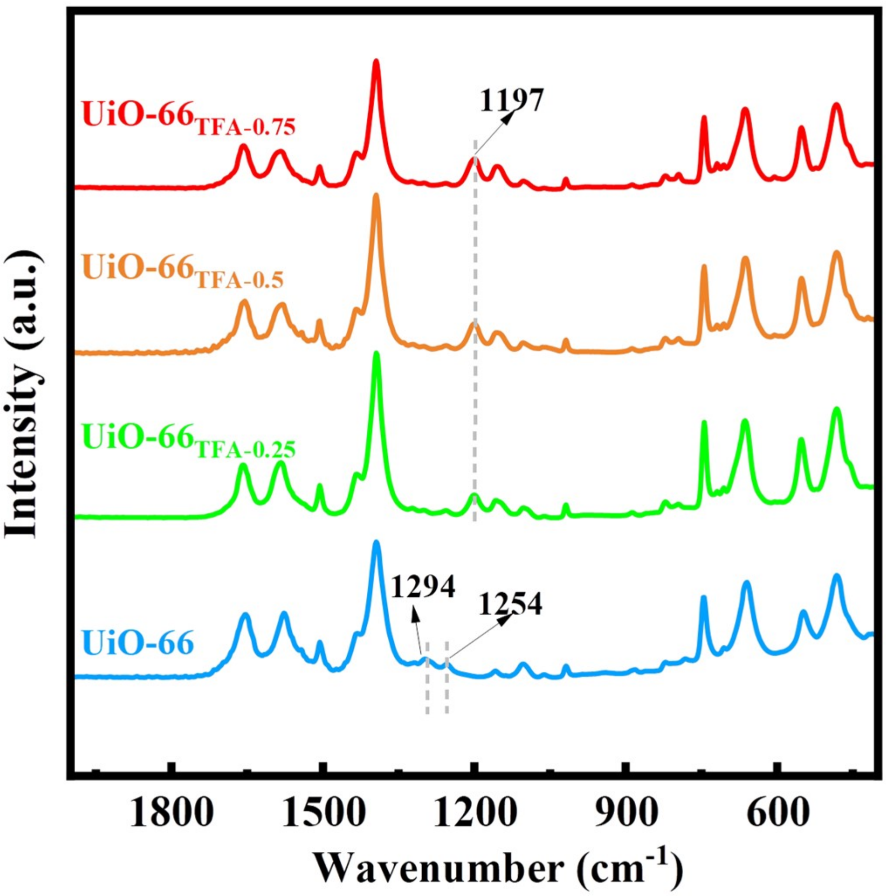

Figure S18. FT-IR spectra of UiO-66$_x$ (UiO-66, UiO-66$_{TFA-0.25}$, UiO-66$_{TFA-0.5}$ and UiO-66$_{TFA-0.75}$).

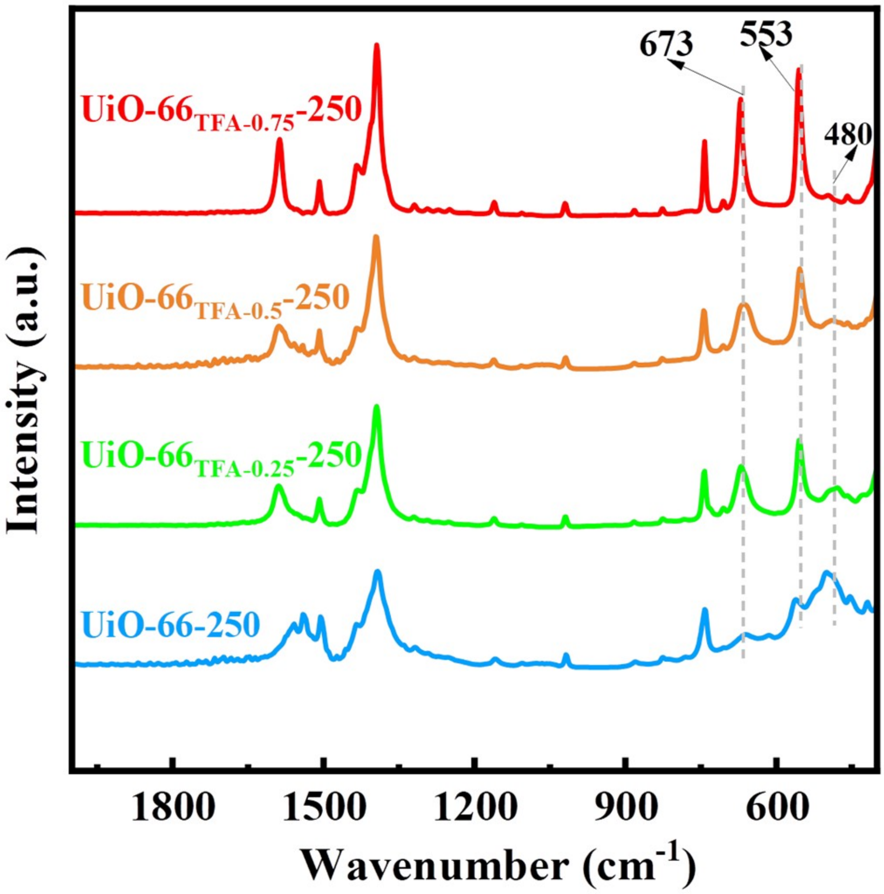

Figure S19. FT-IR spectra of UiO-66$_x$-250 (UiO-66-250, UiO-66$_{TFA-0.25}$-250, UiO-66$_{TFA-0.5}$-250 and UiO-66$_{TFA-0.75}$-250).

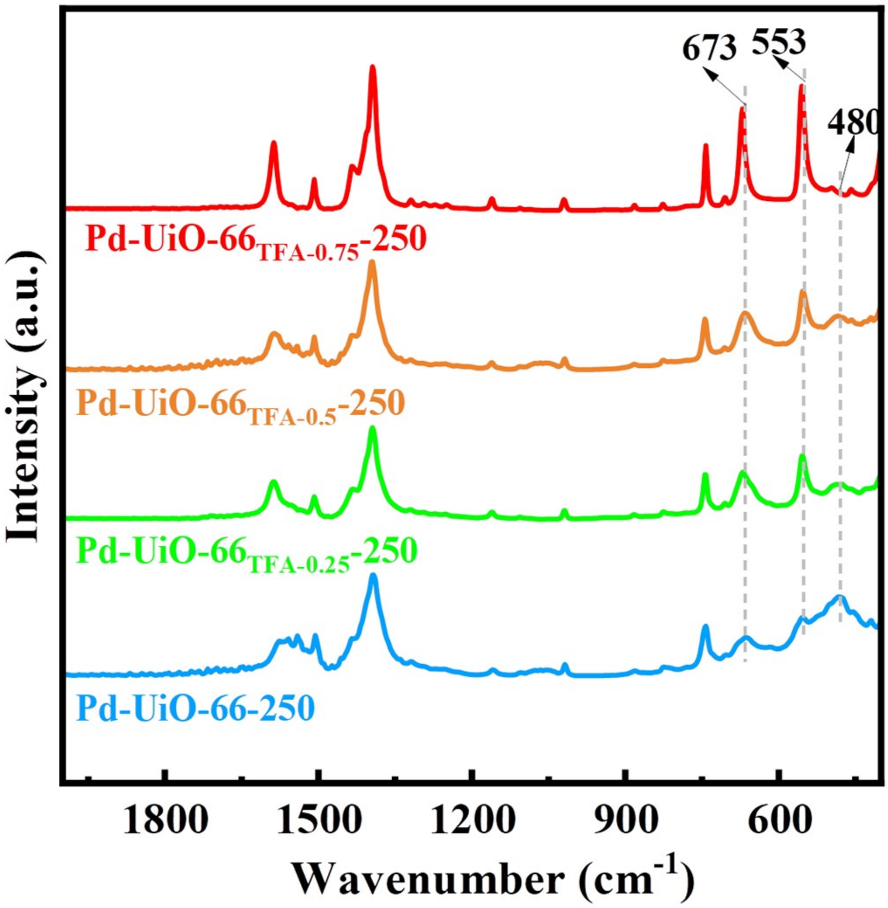

Figure S20. FT-IR spectra of Pd-UiO-66$_x$-250 (Pd-UiO-66-250, Pd-UiO-66$_{TFA-0.25}$-250, Pd-UiO-66$_{TFA-0.5}$-250 and Pd-UiO-66$_{TFA-0.75}$-250).

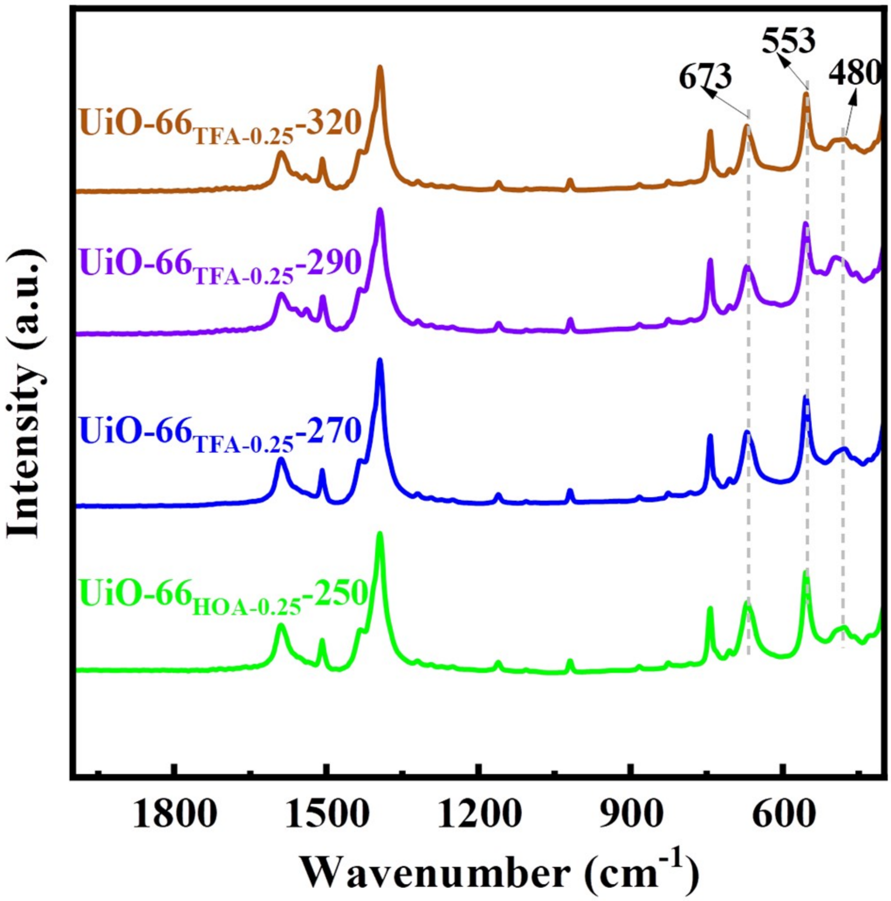

Figure S21. FT-IR spectra of UiO-66$_{TFA-0.25}$-X (UiO-66$_{TFA-0.25}$-250, UiO-66$_{TFA-0.25}$-270, UiO-66$_{TFA-0.25}$-290 and UiO-66$_{TFA-0.25}$-320).

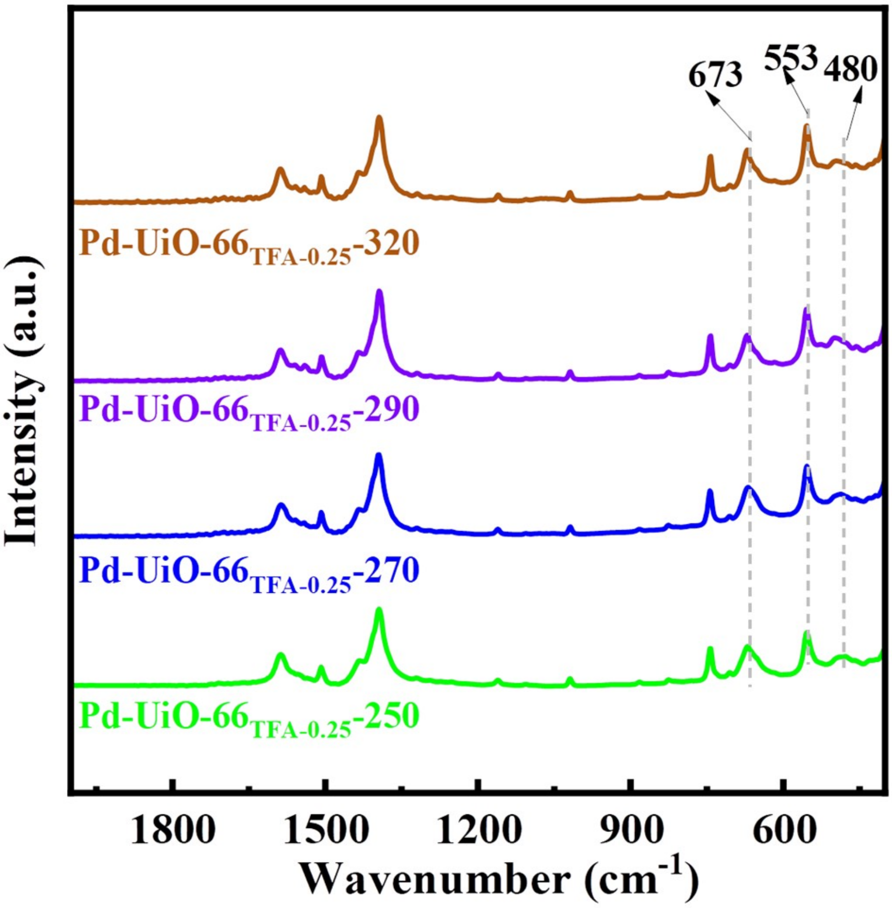

Figure S22. FT-IR spectra of Pd-UiO-66$_{TFA-0.25}$-X (Pd-UiO-66$_{TFA-0.25}$-250, Pd-UiO-66$_{TFA-0.25}$-270, Pd-UiO-66$_{TFA-0.25}$-290 and Pd-UiO-66$_{TFA-0.25}$-320).

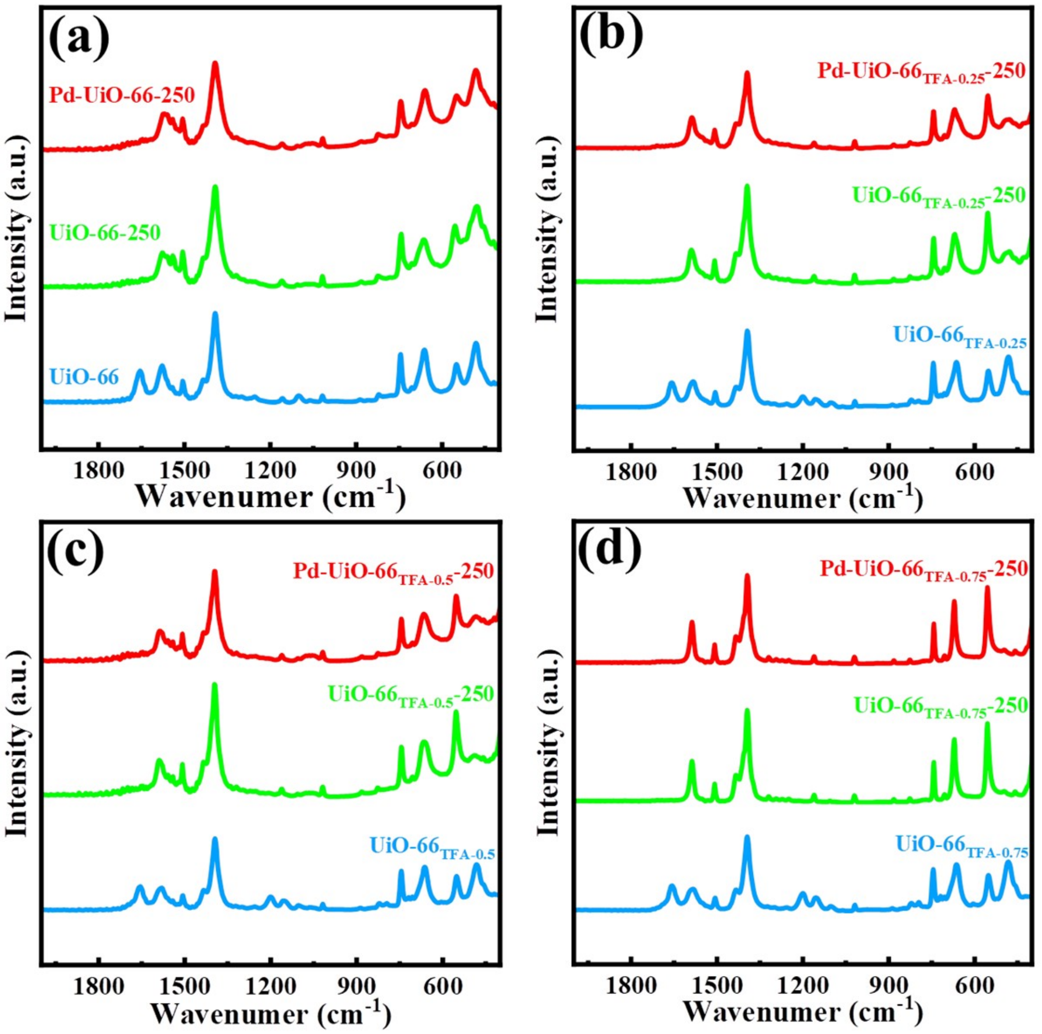

Figure S23. FT-IR spectra of comparison of pristine MOF, activation MOF and Pd-MOF: (a) UiO-66-250, (b) UiO-66$_{TFA-0.25}$-250, (c) UiO-66$_{TFA-0.5}$-250 and (d) UiO-66$_{TFA-0.75}$-250.

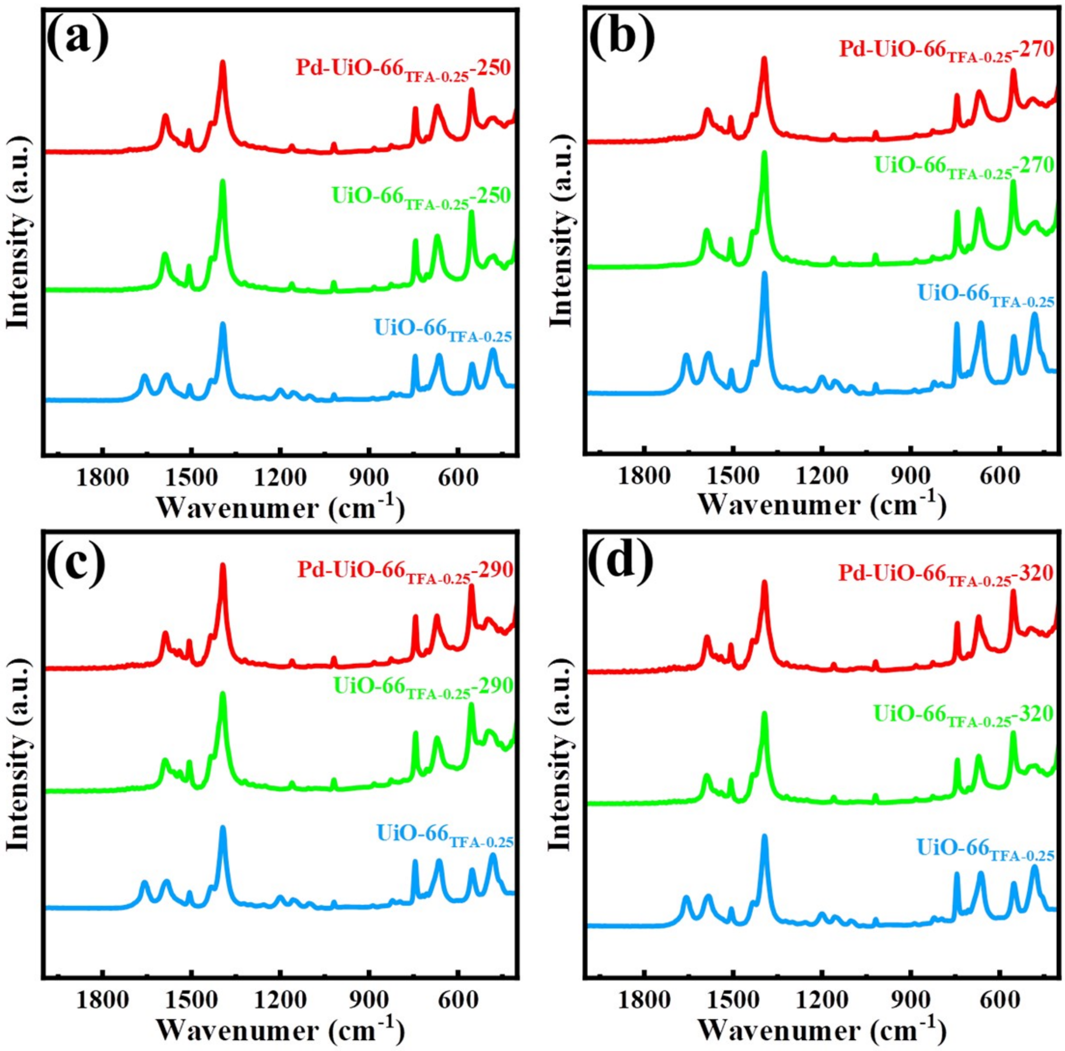

Figure S24. FT-IR spectra of comparison of pristine MOF, activation MOF and Pd-MOF: (a) UiO-66$_{TFA-0.25}$-250, (b) UiO-66$_{TFA-0.25}$-270, (c) UiO-66$_{TFA-0.25}$-290, and (d) UiO-66$_{TFA-0.25}$-320.

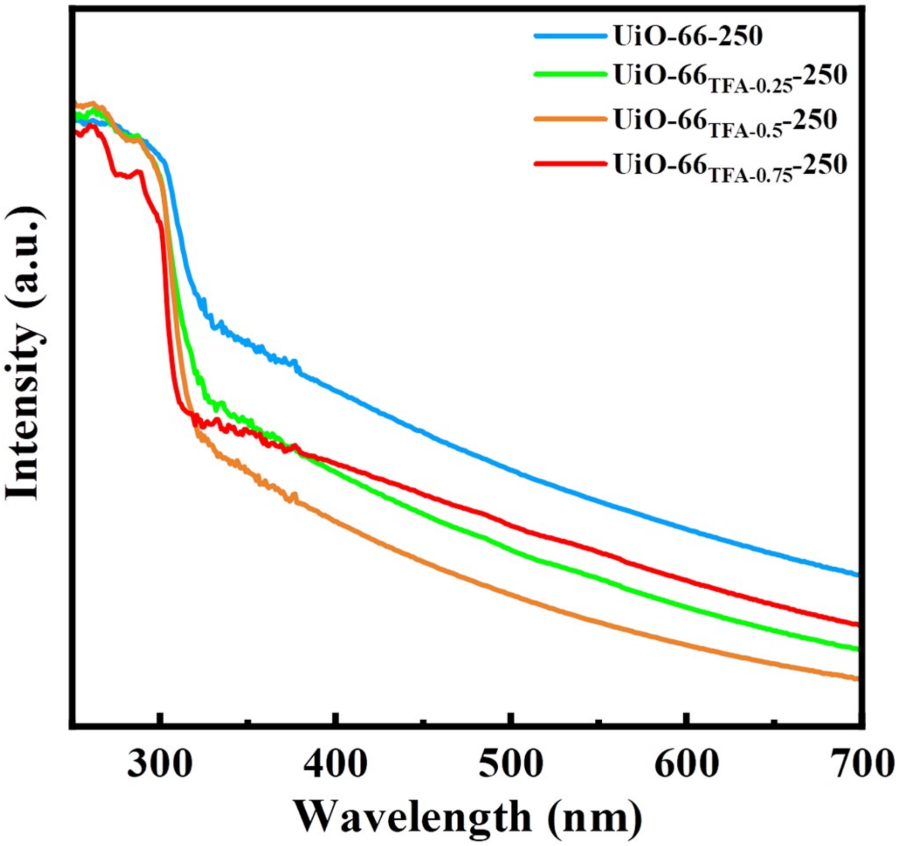

Figure S25. UV-vis diffuses reflectance spectra of UiO-66_x-250.

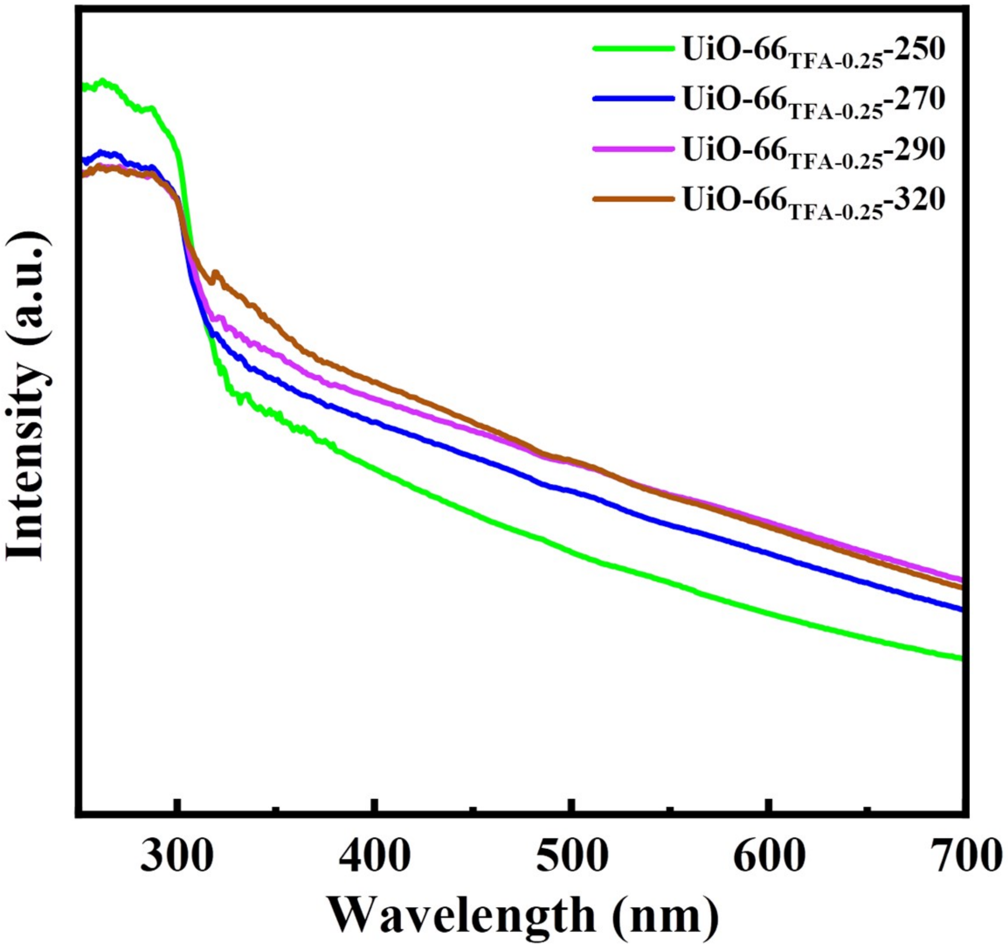

Figure S26. UV-vis diffuses reflectance spectra of UiO-66$_{TFA-0.25}$-X.

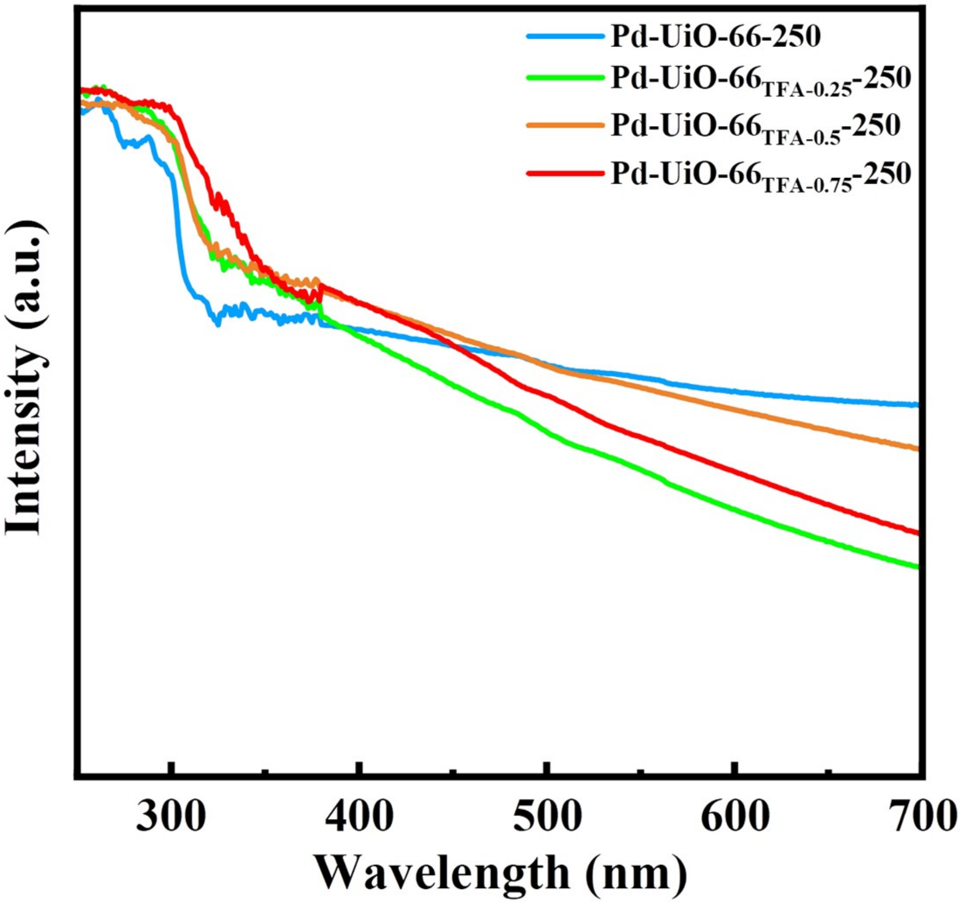

Figure S27. UV-vis diffuses reflectance spectra of Pd-UiO-66$_x$-250.

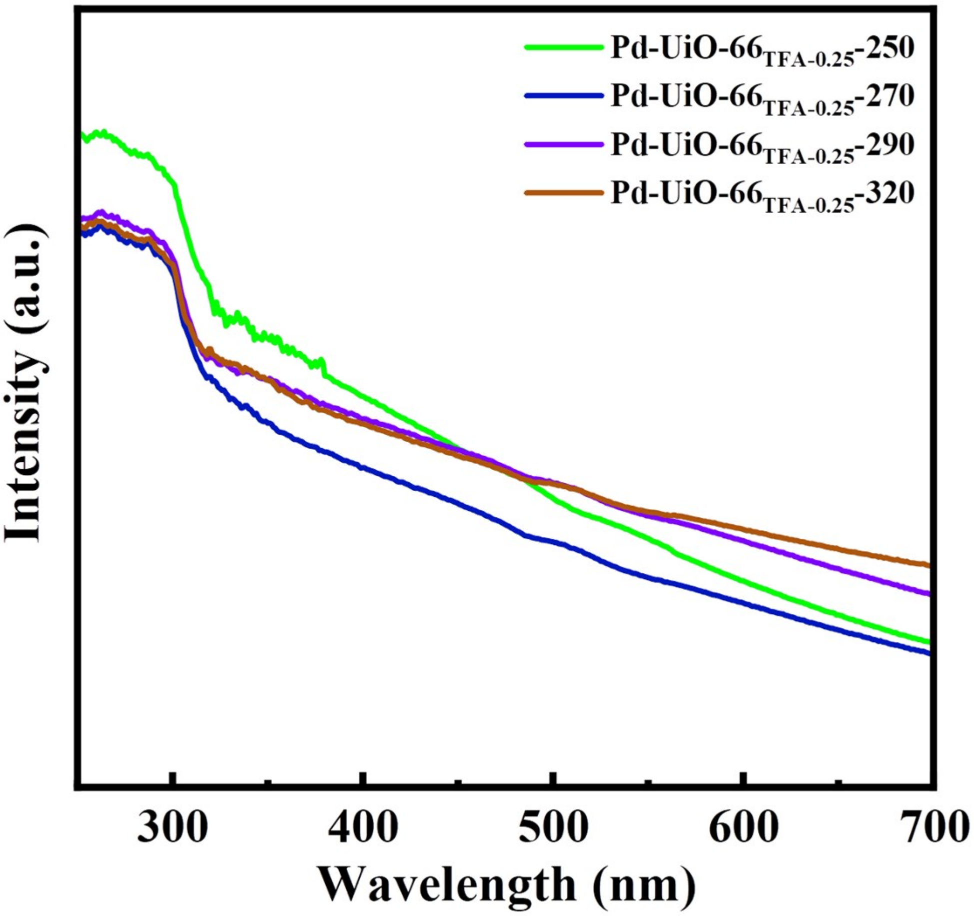

Figure S28. UV-vis diffuses reflectance spectra of Pd-UiO-66$_{TFA-0.25}$-X.

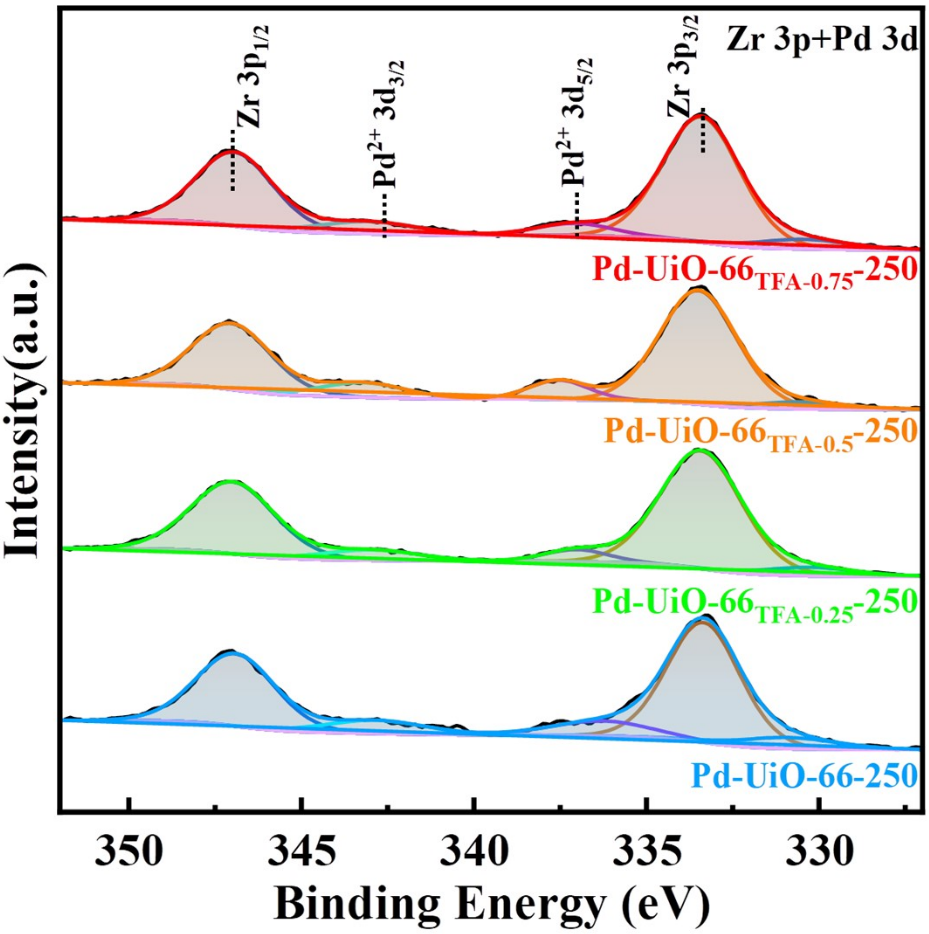

Figure S29. Pd 3d + Zr 3p XPS spectra of Pd-UiO-66$_x$-250.

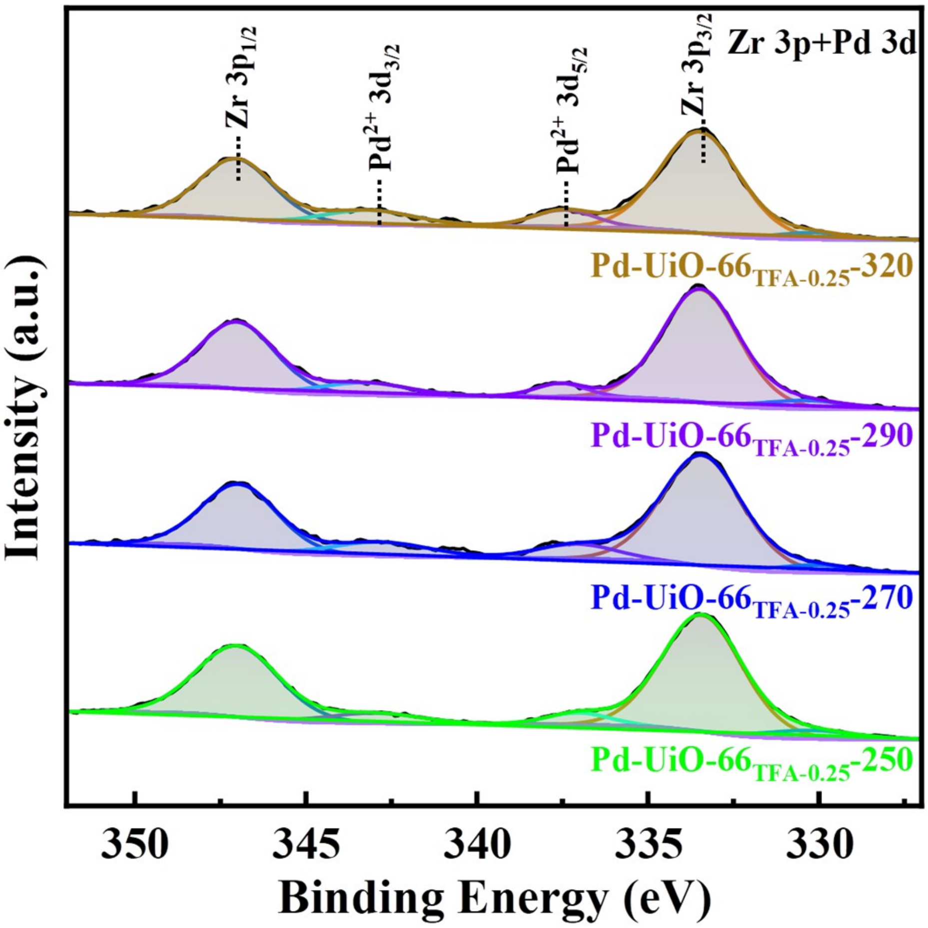

Figure S30. Pd 3d + Zr 3p XPS spectra of Pd-UiO-66$_{TFA-0.25}$-X.

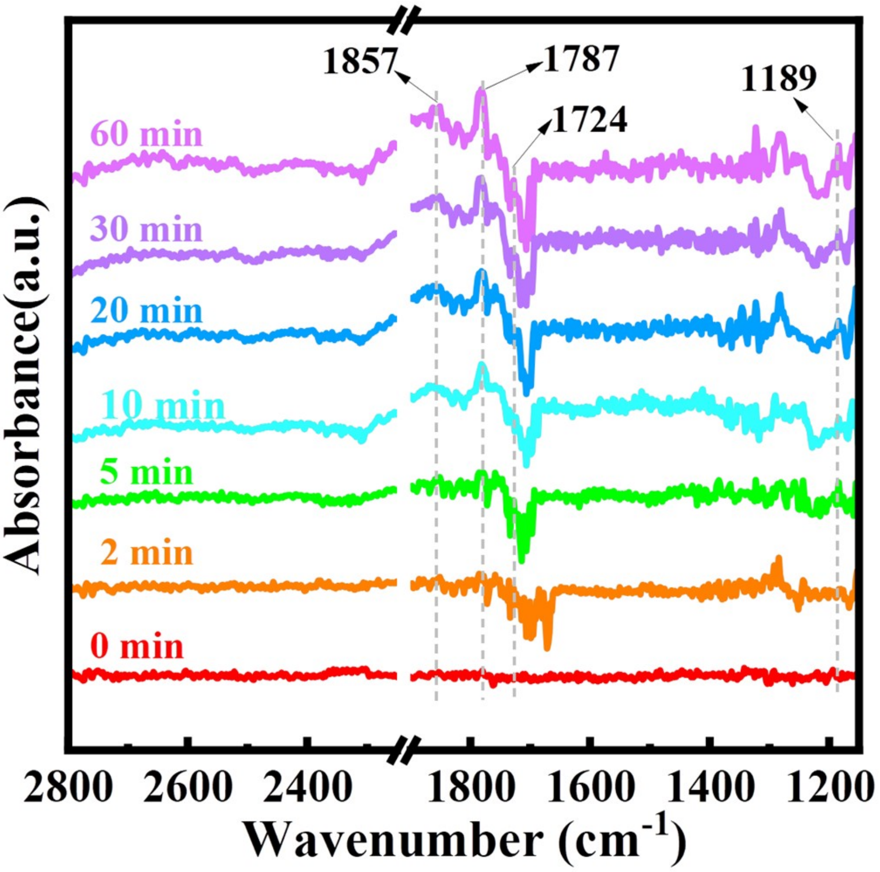

Figure S31. *In situ* DRIFTS spectra on Pd-UiO-66-250 pre-adsorbed with MN under 120^{o}C as a function of CO.

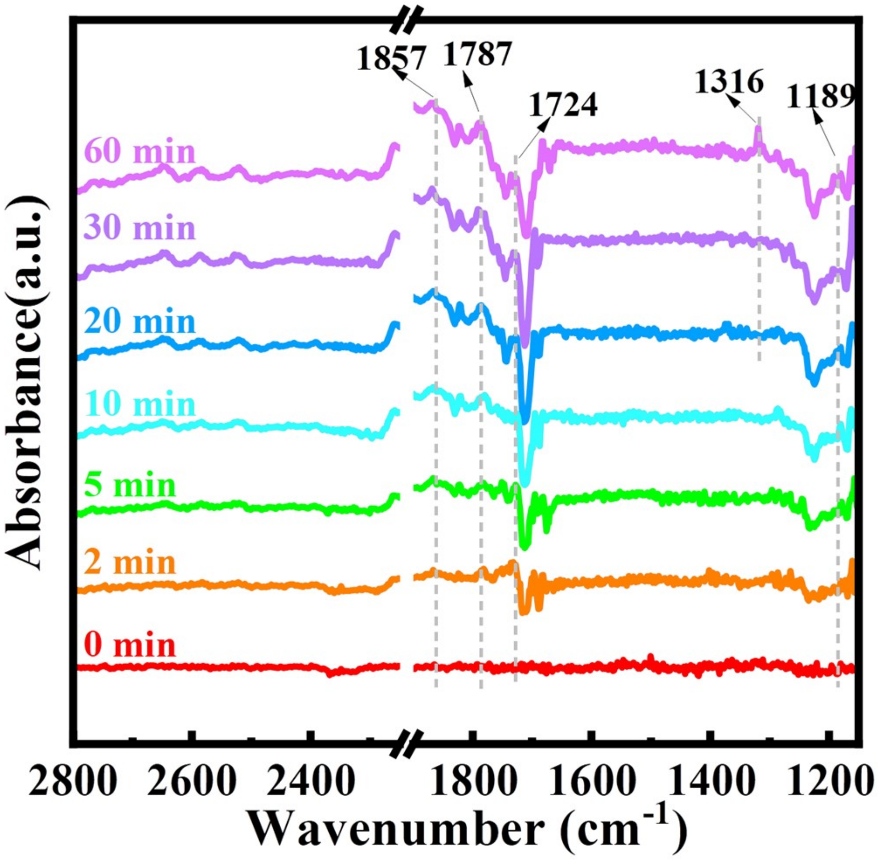

Figure S32. *In situ* DRIFTS spectra on Pd-UiO-66$_{\mathrm{TFA-0.25}}$-290 pre-adsorbed with MN under 120^{o}C as a function of CO.

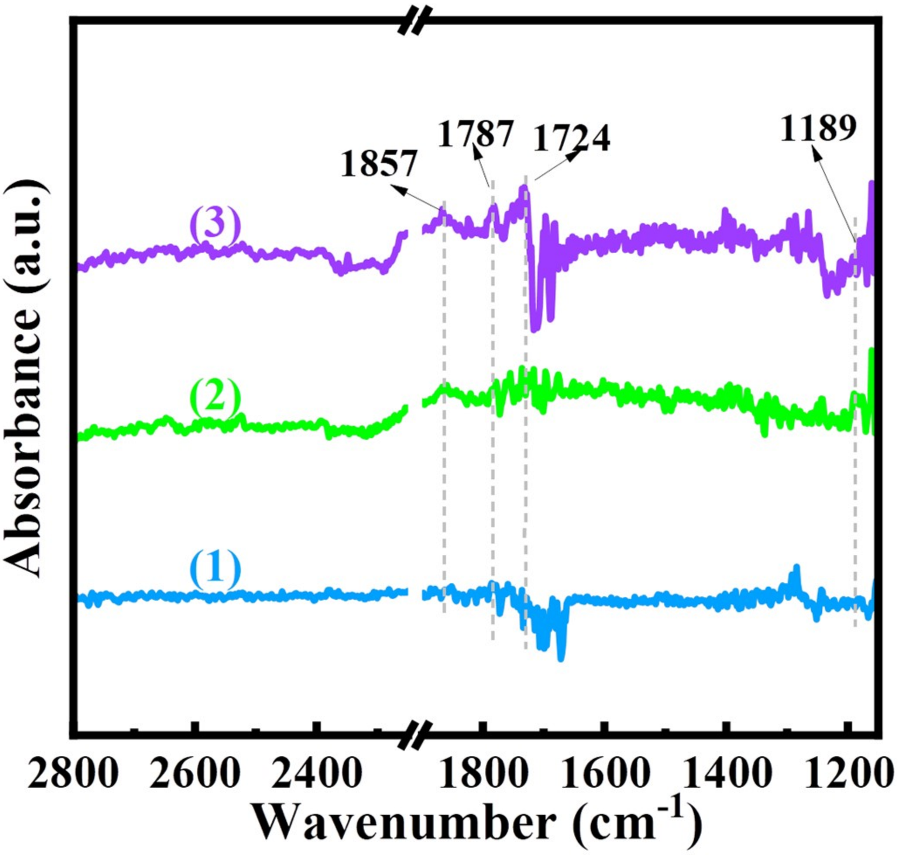

Figure S33. *In situ* DRIFTS spectra on Pd-UiO-66-250 (1), Pd-UiO-66$_{\text{TFA-0.25}}$-250 (2) and Pd-UiO-66$_{\text{TFA-0.25}}$-290 (3) pre-adsorbed with MN under 120^{o}C after exposing CO for 2 mins.

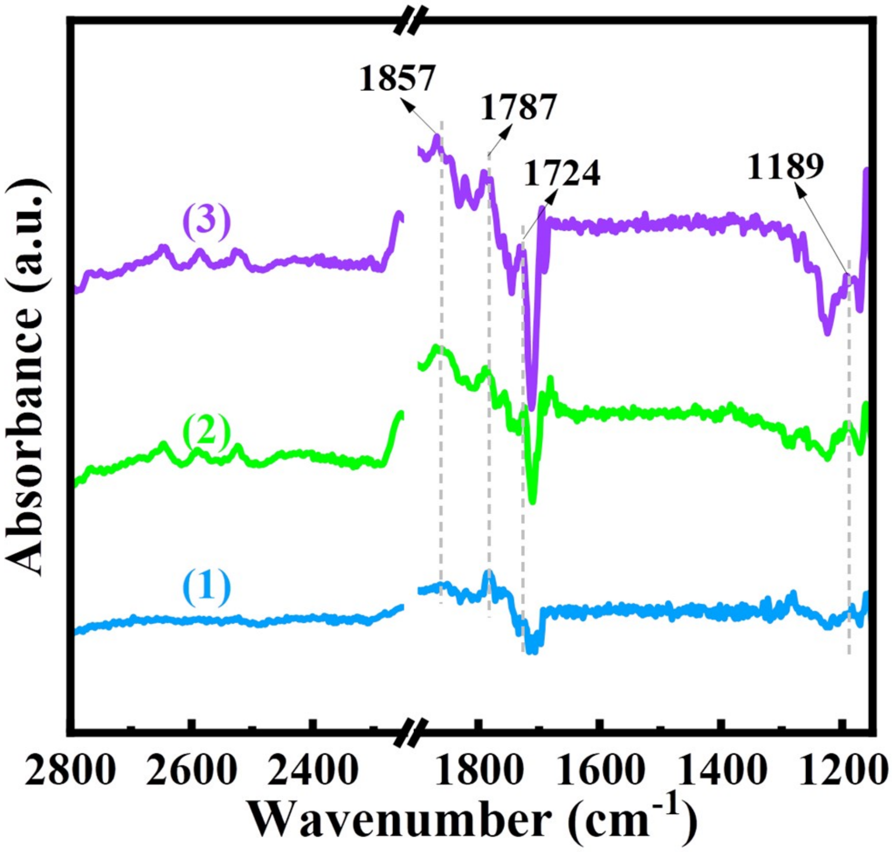

Figure S34. *In situ* DRIFTS spectra on Pd-UiO-66-250 (1), Pd-UiO-66$_{TFA-0.25}$-250 (2) and Pd-UiO-66$_{TFA-0.25}$-290 (3) pre-adsorbed with MN under 120^{o}C after exposing CO for 30 mins.

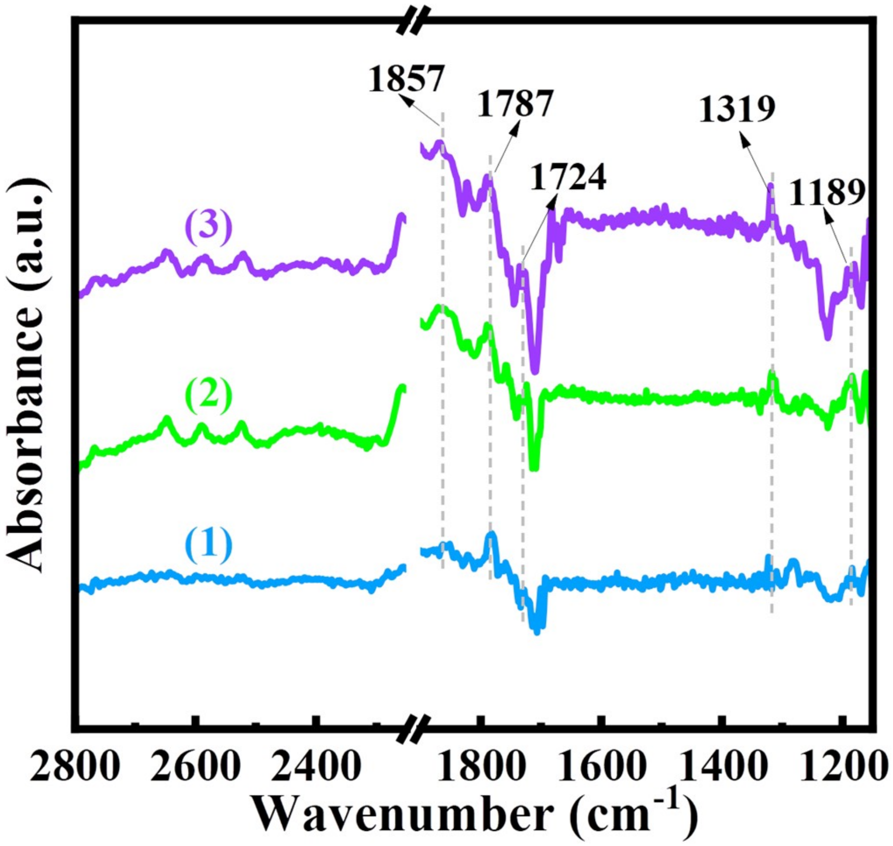

Figure S35. *In situ* DRIFTS spectra on Pd-UiO-66-250 (1), Pd-UiO-66$_{TFA-0.25}$-250 (2) and Pd-UiO-66$_{TFA-0.25}$-290 (3) pre-adsorbed with MN under 120^{o}C after exposing CO for 60 mins.

Table S1. The loading of Pd (II) on the UiO-66$_x$-250 determined by ICP-OES (ICP).

Catalysts	**Pd loading (wt%)**
Pd-UiO-66-250	0.794
Pd-UiO-66$_{\mathrm{TFA-0.25}}$-250	0.82
Pd-UiO-66$_{\mathrm{TFA-0.5}}$-250	0.80
Pd-UiO-66$_{\mathrm{TFA-0.75}}$-250	0.784

Table S2. BET surface area and Langmuir surface area for UiO-66$_{\mathrm{TFA-0.25}}$-250 and Pd-UiO-66$_{\mathrm{TFA-0.25}}$-250.

Supports	**BET Surface Area（m^2g^{-1}）**	**Langmuir Surface Area（m^2g^{-1}）**
UiO-66$_{\mathrm{TFA-0.25}}$-250	934.02	1049.16
Pd-UiO-66$_{\mathrm{TFA-0.25}}$-250	620.98	965.42

Table S3. The loading of Pd (II) on the UiO-66$_{TFA-0.25}$-X determined by ICP.

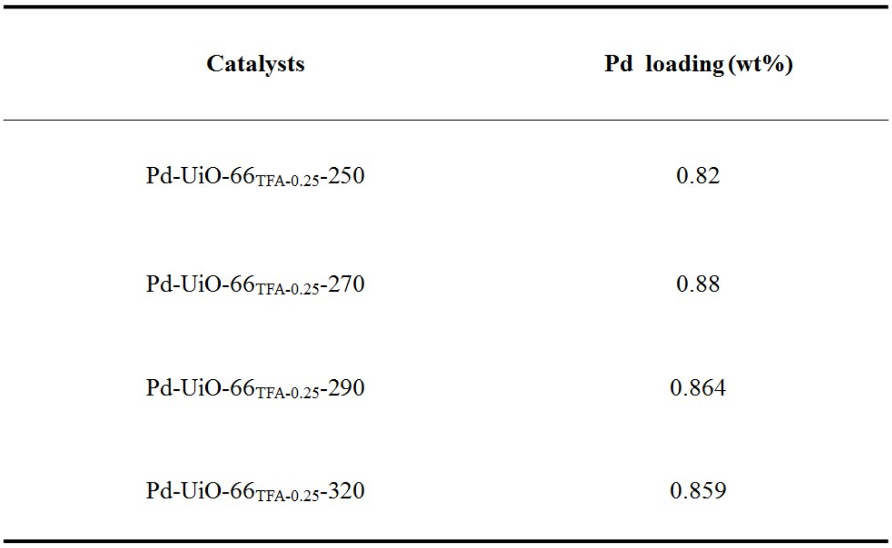

Catalysts	**Pd loading (wt%)**
Pd-UiO-66$_{TFA-0.25}$-250	0.82
Pd-UiO-66$_{TFA-0.25}$-270	0.88
Pd-UiO-66$_{TFA-0.25}$-290	0.864
Pd-UiO-66$_{TFA-0.25}$-320	0.859

Table S4. BET surface area and Langmuir surface area for UiO-66$_x$-250.

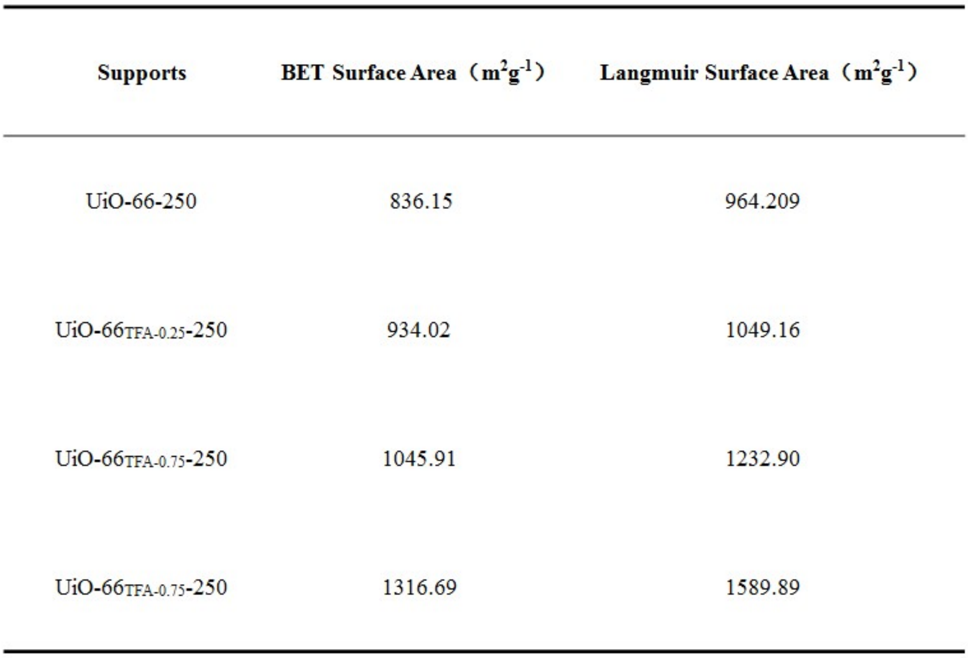

Supports	BET Surface Area（m^2g^{-1}）	Langmuir Surface Area（m^2g^{-1}）
UiO-66-250	836.15	964.209
UiO-66$_{TFA-0.25}$-250	934.02	1049.16
UiO-66$_{TFA-0.75}$-250	1045.91	1232.90
UiO-66$_{TFA-0.75}$-250	1316.69	1589.89

Table S5. BET surface area and Langmuir surface area for UiO-$66_{TFA-0.25}$-X.

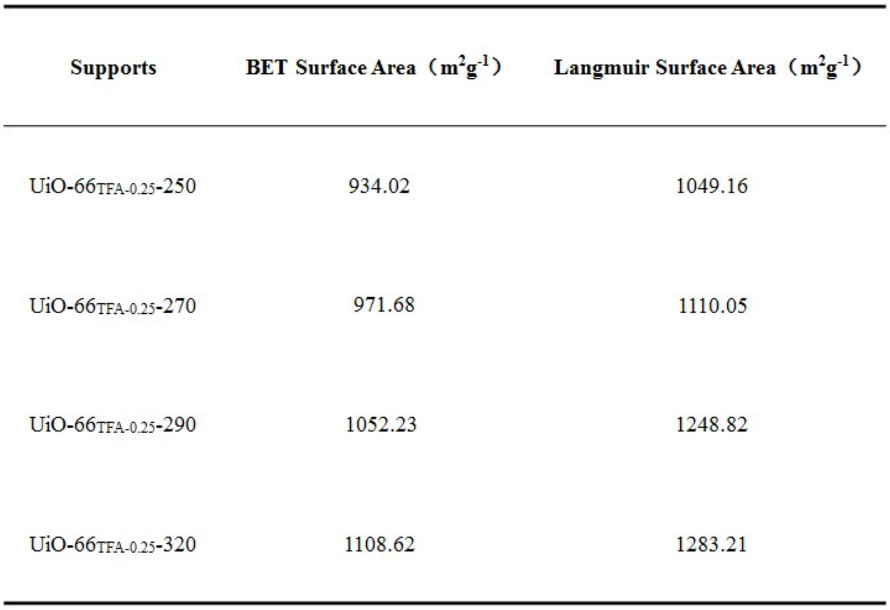

Supports	BET Surface Area（m^2g^{-1}）	Langmuir Surface Area（m^2g^{-1}）
UiO-$66_{TFA-0.25}$-250	934.02	1049.16
UiO-$66_{TFA-0.25}$-270	971.68	1110.05
UiO-$66_{TFA-0.25}$-290	1052.23	1248.82
UiO-$66_{TFA-0.25}$-320	1108.62	1283.21

Table S6. CO-TPD peaks analysis of the Pd-UiO-66$_x$-X.

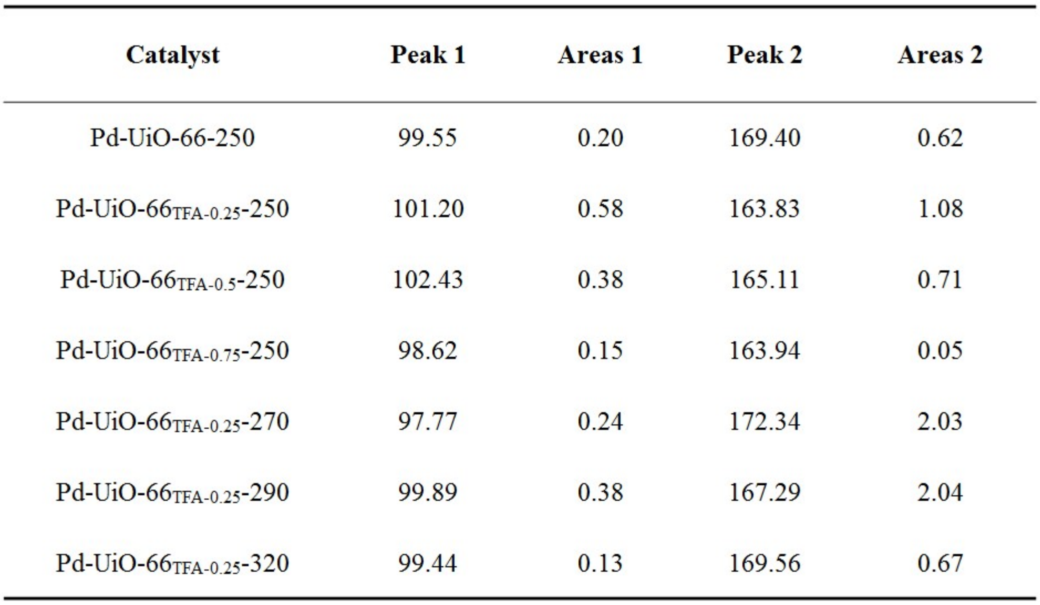

Catalyst	**Peak 1**	**Areas 1**	**Peak 2**	**Areas 2**
Pd-UiO-66-250	99.55	0.20	169.40	0.62
Pd-UiO-66$_{\text{TFA-0.25}}$-250	101.20	0.58	163.83	1.08
Pd-UiO-66$_{\text{TFA-0.5}}$-250	102.43	0.38	165.11	0.71
Pd-UiO-66$_{\text{TFA-0.75}}$-250	98.62	0.15	163.94	0.05
Pd-UiO-66$_{\text{TFA-0.25}}$-270	97.77	0.24	172.34	2.03
Pd-UiO-66$_{\text{TFA-0.25}}$-290	99.89	0.38	167.29	2.04
Pd-UiO-66$_{\text{TFA-0.25}}$-320	99.44	0.13	169.56	0.67

References

1. A. M. Hastings, D. Ray, W. Jeong, L. Gagliardi, O. K. Farha and A. E. Hixon, Advancement of Actinide Metal–Organic Framework Chemistry via Synthesis of Pu-UiO-66, *J. Am. Chem. Soc.*, 2020, **142**, 9363-9371.
2. S. Ghosh and S. Biswas, Ultrafast and Nanomolar Level Detection of H_2S in Aqueous Medium Using a Functionalized UiO-66 Metal–Organic Framework Based Fluorescent Chemosensor, *Dalton Trans.*, 2021, **50**, 11631-11639.
3. Y.-P. Xu, Z.-Q. Wang, H.-Z. Tan, K.-Q. Jing, Z.-N. Xu and G.-C. Guo, Lewis Acid Sites in MOFs Supports Promoting the Catalytic Activity and Selectivity for CO Esterification to Dimethyl Carbonate, *Catal. Sci. Technol.*, 2020, **10**, 1699-1707.
4. F. Vermoortele, B. Bueken, G. Le Bars, B. Van de Voorde, M. Vandichel, K. Houthoofd, A. Vimont, M. Daturi, M. Waroquier, V. Van Speybroeck, C. Kirschhock and D. E. De Vos, Synthesis Modulation as a Tool to Increase the Catalytic Activity of Metal-Organic Frameworks: The Unique Case of UiO-66(Zr), *J. Am. Chem. Soc.*, 2013, **135**, 11465-11468.